STRATEGIES FOR COMPUTING THE SCALAR SELF-FORCE ON A
SCHWARZSCHILD BACKGROUND: A COMPARISON STUDY WITH AN FORTRAN
CODE IN C++, EXTRAPOLATING TO INFINITE DISCONTINUOUS GALERKIN
ORDER, AND EXTRAPOLATING TO INFINITE SPHERICAL HARMONIC MODES

A General Exam Paper

Submitted to the Graduate Faculty of the
Louisiana State University and
Agricultural and Mechanical College
in partial fulfillment of the
requirements for the degree of
Ph D

in

Physics

by
Steven (Susan) Dorsher
B.S., Massachusetts Institute of Technology, 2004
M.S., The Ohio State University, 2006
M.S., University of Minnesota, 2013
December, 2017

Acknowledgments

I would like to thank Peter Diener and Frank Löffler for their guidance. Peter Diener especially has been very important to me, both as an advisor and personally. Frank Löffler and the Einstein Toolkit grant has also provided some of the funding for this research, and I would like to thank him for that and for all of his help. I would also like to thank Gabriela Gonzalez for the excellent opportunity to work on LIGO during the time of three detections, which provided me the funding I needed to continue the work detailed in this document. I would like to thank Juana Moreno for the opportunity to work as outreach coordinator to the LA-SIGMA Research Experience for Undergraduates program my first summer at LSU, which also helped provide funding for this research. My parents, Paul and Joanne Dorsher, also deserve a mention, both for extraordinary moral support and for the financial support they provided that helped make this possible. My family, friends, and loved ones are the purpose behind this work.

Table of Contents

List of Tables

List of Figures

Abstract

In this document, I present the results of one comparison study in which I reproduce Peter Diener's simulation [18] of a scalar particle on a Schwarzschild background for the purpose of producing Extreme Mass Ratio black hole binary templates for the Laser Interferometer Space Antenna. Porting this Fortran code to C++ has provided an independent verification of the code to roundoff precision. The results do not verify, but are consistent with, Wardell et al.'s circular orbit results from 2012 using a different differencing scheme [?]. I present preliminary results from a second comparison study of Niels Warburton's and Peter Diener's and Barry Wardell's scalar self-force simulation for eccentric orbits. These results are so far consistent with the physical reasoning gained from Field, Hesthaven, and Lau [?]; with the caveat that their results are for the gravitational case while ours are for the scalar case. Finally, I make use of a first order Richardson extrapolation to obtain the self-force at infinite Discontinuous Galkerin order then sum the spherical harmonic modes to obtain the total self-force as a function of time. The long term goal is to continue the second comparison study with self-consistent evolution.

Chapter 1
Introduction

1.1 Gravitational Waves

On February 11, 2016, the LIGO Scientific Collaboration announced the first detection of gravitational waves from a black hole binary inspirals, occurring on September 14, 2015, with pre-merger masses of 36 $M_\odot$ and 29 $M_\odot$ and a post merger mass of 62 $M_\odot$ at a redshift of $z = 0.09$ [21]. Two subsequent detections followed, on December 26, 2015 [22] and on January 4, 2017 [23], with masses that are about the same to within an order of magnitude. This detection was well-anticipated. Russel Hulse and Joseph Taylor were awarded the Nobel Prize in 1993 for their 1974 discovery of a binary pulsar. This, and similar pulsars yielded precise timing measurements of orbital period changes that corresponded to rates expected due to gravitational wave emission [8]. Stellar mass black holes have been known observationally for some time since the discovery of the x-ray source Cygnus X-1 in the 1960's. Active galactic nuclei at the center of galaxies have been identified as supermassive black holes since the 1960's as well. Saggitarius A^*, a supermassive black hole at the center of the Milky Way, was originally identified through radio astronomy and is also observable in the X-ray [61], but its black hole nature has been confirmed most precisely through a 16 year study of the orbits of neighboring stars [13].

All known stellar mass black holes from x-ray sources are spinning [3], the LIGO gravitational wave detections suggested or were consistent with spinning black holes [21] [22] [23], and theoretical expectations are that angular moment from the black hole formation process should be deposited in the newly formed black hole, leaving it spinning, for the case of stellar mass black holes. For the case of supermassive black holes, there are multiple formation scenarios. One model suggests that they form from mergers of massive mass black holes from the deaths of Population I stars. Another model suggests that they are formed from large scale structure collapsing first along one dimension, then subsequently

along the other two, followed by mergers into larger black holes. The third model suggests a mechanism involving initial black hole seeds at scales between these two, formed from collapsing "clouds" in the galactic disk. All of these models impart some spin to the initial seed black hole, that may or may not be retained in subsequent mergers [54]. For the purposes of this document, I consider black holes without spin, using the Schwarzschild metric.

1.2   Extreme Mass Ratio Inspirals

In an extreme mass ratio inspiral (EMRI), a stellar mass black hole, or other compact object such as a white dwarf or neutron star, orbits around a supermassive black hole. It emits energy due to gravitational waves and its orbital frequency gradually increases while its orbital radius gradually decreases. Eventually it crosses the innermost stable circular orbit and, assuming it is on a roughly circular orbit, it plunges into the black hole without completing any further orbits. Picture this in the presence of a negligible accretion disk, or inside the inner edge of the accretion disk, or out of the orbital plane of the accretion disk.

The stellar mass black hole can be a factor of 10^5 to 10^6 smaller than the mass of the supermassive black hole in an EMRI. In an intermediate mass ratio inspiral (IMRI), the mass ratio is more like 10^2 to 10^4. LISA will be sensitive to EMRI's and some IMRI's. LIGO may be sensitive to some IRMI's. It is our goal to enable to the LISA community to provide gravitational wave templates to the LISA searches in time for the LISA launch in the early 2030's. Extraordinary precision is required to perform these searches, requiring an error in the period of no more $\delta P/P < 10^{-6}$ [7]. This is especially challenging given that the EMRI system must be evolved over a much longer timescale than a single period due to the persistence of the initial conditions in the system and will be much longer than a single period for any physical system. This timescale scales as M/μ, where M is the central black hole mass and μ is the mass ratio. For a mass ratio of 10^5, approximately 10^5 wave-cycles must be evolved [7].

1.3 Self force

Consider a classical model of the atom. This is more like the Bohr model than the plum pudding model, but it doesn't make any attempt at quantization. A negatively charged electron is orbiting a positively charged nucleus. That electron emits radiation and loses energy, becoming more tightly bound. The force that causes it to move inward is called the self-force, because it is the force of the particle interacting with its own electric field [10].

The self-force also exists in general relativity. In the simplest possible picture of general relativity, a test particle experiencing no force moves on a geodesic. However, once we bring into our picture the the principle that the small particle (now a stellar mass black hole) has mass– any amount of mass– it also curves space-time, generating a back-reaction. It is possible to obtain the self-force in general relativity from either perturbations of the metric [?] or perturbations of the particle's world-line [56]. Either way, the small parameter governing the expansion is the mass ratio of the system. Again, the self-force is due to the interaction of the small black hole with the gravitational field itself.

In this document, we consider a slightly simpler problem, that of a scalar field on a curved space-time background. In this case, the self-force is still due to the interaction of the scalar field with the particle itself. The stellar mass black hole is now a scalar delta function source that evolves along an orbit through space-time. As in the other two cases, the source causes scalar waves to be emitted that travel in all spatial directions away from the source, both toward light-like infinity and into the supermassive black hole horizon. The back-reaction causes a self-force that propels the particle slightly inward with each orbit as it loses energy to these outgoing waves. Ultimately, if evolved for that long, the particle should enter the horizon of the large black hole and then, it is beyond the scope of present day physics to say what should happen to it.

1.4 The gravitational wave sky

Currently, there are four distinct windows on the gravitational wave universe planned or in progress. The Laser Interferometer Gravitational Wave Observatory, LIGO, probably deserves first listing, due to their recent success. LIGO observes gravitational waves using a ground based Michelson-Morley interferometer with two 4 kilometer long Fabry-Perot cavity arms. It detects strains as small as $10^{-23}Hz^{-1/2}$ [35]. It has thus-far had three detections of black hole binary pairs in the tens of solar mass range. These mergers have been tracked through inspiral and merger [21] [22] [23], and ringdown [28], to produce exact tests of general relativity. LIGO has even been able to set limits on non-General Relativistic behavior, such as the magnitude of the dispersion of the intergalactic medium to gravitational waves [23] and deviation of the post Newtonian parameters from those predicted from GR [28]. The LIGO-Virgo collaboration continues searches for neutron star binary inspirals, which may have electromagnetic counterparts in the form of supernovae; pulsars, which are thought to have raised "mountains" their surface causing a changing quadrapole moment– these will also have electromagnetic counterparts; gravitational wave bursts correlated with EM, neutrino, or particle sources such as a gamma ray burst; or the cosmic or galactic white dwarf binary stochastic background radiation. In the future, KAGRA, an observatory in Japan, and IndIGO, an observatory in India, will join the search for gravitational waves, refining the collaboration's ability to locate a source on the sky. Geo600 is an existing English gravitational wave detector in England. The Einstein Telescope is a next generation gravitational wave detector that has also been proposed.

The cosmic microwave background (CMB) can also be used to constrain the primordial stochastic background of gravitational waves. It is a very low frequency source, with wavelengths related to the size of the observable universe ($f \sim 10^{-17}Hz$). Searches depend upon separating the polarization into two components: the B-modes, which have curl, and the E-modes, which don't. If the B-modes and the E-modes are roughly even, then tensor components of the density perturbation dominate, and gravitational waves may

be present. Micro-lensing and dust are significant noise sources that must be carefully subtracted. Current searches include BICEP2, Planck, and the Keck Array. Planned ground and balloon borne experiments include the ACTPol, Polarbear, CLASS, Piper, and Spider. Planned space-base experiments include COrE, PRISM, LiteBIRD, and PIXIE [16].

Pulsar timing uses the extremely precise timing of pulsars, taking their spin down into account and correlating with pairs of other pulsars. In this timing, they are looking for residual signals that may be due to supermassive black hole binaries, cosmic string cusps, and the cosmic stochastic gravitational wave background. Existing pulsar timing arrays include the Parkes Pulsar Timing Array (PPTA), the Eurpeoan Pulsar Timing Array (EPTA), and the North American Nanohertz Observatory for Gravitational Waves (NANOGrav). They have formed a collaboration called the International Pulsar Timing Array (IPTA). The IPTA is sensitive from 10^{-9} to 5×10^{-8} Hz with strains on the order of 10^{-14} to 10^{-15} [20].

Extreme mass ratio black hole binaries are likely to be detected only by LISA. The Laser Interferometer Space Observatory (LISA) is a space-based observatory.Like LIGO, it will use interferometry to detect gravitational waves; however, it will have three arms arranged in a triangle separated by 2.5 million kilometers. Each end mirror will be in free-fall on a satellite, with the satellite stabilized by micro-thrusters. LISA Pathfinder was launched in 2015 and demonstrated the optics essential to this space-based mission can operate successfully remotely. As of June of 2017, LISA is fully funded by the European Space Agency, with a NASA as a lesser partner. The launch date is set in the early 2030's. In addition to EMRI's, LISA may detect IMRI's, supermassive black hole binaries, and the primordial stochastic gravitational wave background.

1.5   Notation

In this manuscript, I use Einstein summation notation for tensors, where a repeated Greek index implies a summation over that repeated index. For example, an n dimensional

tensor field of rank (1,2) transforms, in general, according to the rule

$$T^{\alpha}_{\beta\gamma}(\bar{x}^1,\ldots,\bar{x}^n) = \Lambda^{\alpha}_{\delta}\Lambda^{\epsilon}_{\beta}\Lambda^{\zeta}_{\gamma}T^{\delta}_{\epsilon\zeta}(x^1,\ldots,x^n) \tag{1.1}$$

where Λ is the Jacobean of the coordinate transformation from x to $\bar{x}$.

Indices are raised by use of the inverse metric and lowered by use of the metric. The metric transforms contravariant one-forms, which constitute the basis, to covariant vectors, which constitute the coordinates, e.g. $u^{\beta} = g^{\alpha\beta}u_{\beta}$, where $g^{\alpha\beta}$ is the metric. However, the metric and its inverse can also be used to raise and lower indices of tensors of higher and mixed rank. The metric describes the relative distance between two coordinates on a manifold, in all n dimensions, in an $n \times n$ matrix. Two sign conventions are allowed, depending on whether the time component is positive or negative, though the metric always has a negative determinant in four dimensions. In our sign convention, the Minkowski metric for flat space-time is given by

$$\eta^{\mu\nu} = \begin{bmatrix} -1 & 0 & 0 & 0 \\ 0 & 1 & 0 & 0 \\ 0 & 0 & 1 & 0 \\ 0 & 0 & 0 & 1 \end{bmatrix}$$

Here the four dimensions are Cartesian, t, x, y, and z. The Schwarzschild metric for a spherically symmetric black-hole without charge or spin is given by

$$d\tau^2 = g^{\mu\nu} \begin{bmatrix} -(1-\frac{2M}{r}) & 0 & 0 & 0 \\ 0 & (1-\frac{2M}{r})^{-1} & 0 & 0 \\ 0 & 0 & r^2 & 0 \\ 0 & 0 & 0 & r^2\sin^2\theta \end{bmatrix}$$

where $d\tau$ is the proper time, and coordinates are t (the local time), r (a radial coordinate

that goes to zero at the singularity, $2M$ at the horizon, and infinity at spatial infinity), θ (the polar angle), and ϕ (the azimuthal angle). To obtain the inverse (lowered) metric, simply invert the matrix representation.

Chapter 2
A simple numerical solution for a PDE using the Discontinuous Galerkin method

2.1 Reduction to coupled first order differential equations

The fundamental problem we wish to solve is to evolve the wave equation on Schwarzschild space-time with a source. However, to begin to address this problem, I implemented a one dimensional wave equation solver in C++ using the Discontinuous Galerkin method in flat space-time. The wave equation in flat space-time is given, in several different forms, by

$$\Box \psi = 0 \tag{2.1}$$

$$\frac{\partial^2 \psi}{\partial t^2} = \nabla \psi \tag{2.2}$$

$$\frac{\partial^2 \psi}{\partial t^2} = \frac{\partial^2 \psi}{\partial r^2} \tag{2.3}$$

where the final form is specialized to one dimension. To numerically integrate this, it is necessary to reduce this second order differential equation to three coupled differential first order differential equations. There is a classical solution to this problem, which we follow. We introduce variables $\rho = \frac{\partial \psi}{\partial t}$ and $\phi = \frac{\partial \psi}{\partial r}$. With these definitions, and remembering that we want time evolution equations rather than spatial evolution equations, the three coupled equations become

$$\frac{\partial \psi}{\partial t} = \rho \tag{2.4}$$

$$\frac{\partial \rho}{\partial t} = \frac{\partial \phi}{\partial r} \tag{2.5}$$

$$\frac{\partial \phi}{\partial t} = \frac{\partial \rho}{\partial r} \tag{2.6}$$

This system of equations can be rewritten

$$\frac{\partial u}{\partial t} = A\frac{\partial u}{\partial r} + B\frac{\partial u}{\partial t} = RHS(u, t)$$

where u is the state vector consisting of $u = (\psi, \rho, \phi)$, and A and B are matrices. RHS stands for Right Hand Side. The C++ code has been implemented for wave equations of this generalized form, which encompasses wave equations on a Schwarzschild space-time.

2.2 Method of Lines

The method of lines is a method for solving partial differential equations in which spatial dimensions are discretized and time (conventionally) is evolved with numerical integration. We use this technique to solve the wave equation.

2.2.1 Spatial grids

Our code solves a wave equation, which must first calculate a spatial derivative then integrate in time to solve a differential equation. For the spatial derivative part of the scheme, we make use of the Discontinuous Galerkin method to compute spatial derivatives, as a replacement for a finite difference scheme. Its has three primary benefits. One is that it naturally handles discontinuities in the evolved field, which is important to the effective source approach that we use when calculating orbits with a source in curved space-time. The second is that its accuracy scales exponentially with increasing polynomial order. The third is that its accuracy scales as a power law with decreasing element size, giving a second strong way to reduce the truncation error.

- **Finite difference schemes**

The classic solution to the spatial derivative problem is the finite difference scheme. In a one dimensional finite difference scheme, space is discretized into points on a line. The spatial derivative is calculated using a stencil of points that is symmetric about the point where one wants to know the spatial derivative, and extends $n-1$ points beyond to either side, where n is the order of the expansion. The spatial derivative is calculated from a

weighted sum of the points included in the stencil, where some of the weights are negative. A stencil with $2n - 1$ points in it, in one dimension, corresponds to an nth order expansion. It is possible to expand any order of derivative to any order of expansion. A first derivative, to second order accuracy, given by:

$$D_r^{(2)} = \frac{1}{h}(-\frac{1}{2}f_{-1} + \frac{1}{2}f_1) \tag{2.7}$$

Here the f_{-1} and f_1 indicate the function evaluated at the grid point to either side of the 0th grid point, where the derivative is evaluated. Here h is the spacing between grid points. A first derivative, to third order accuracy, is given by:

$$D_r^{(3)} = \frac{1}{h}(\frac{1}{12}f_{-2} - \frac{2}{3}f_{-1} + \frac{2}{3}f_1 - \frac{1}{12}f_2) \tag{2.8}$$

Notice how no first order derivative includes the central point in its stencil. In contrast, a second derivative to second order accuracy is given by:

$$D_r'^{(2)} = \frac{1}{h^2}(f_{-1} - 2f_0 + f_1) \tag{2.9}$$

This derivative is symmetric, while the first derivative is antisymmetric.

It is possible to extend these stencils to two and three dimensions. When considering parallelization using OpenMP, issues of synchronization must be considered. When parallelizing over many nodes, the spatial grid gets divided into blocks. At the ends of each block, the boundary cells need information from the neighboring cells to calculate the spatial derivative. For an order n derivative, $n - 1$ boundary cells are synchronized into buffer zones both to the left and to the right at each time step. In our code, this is not necessary, since we have parallelized with OpenMP, which uses shared memory within one node, across several (16) cores.

- **The Discontinuous Galerkin method**

The Discontinuous Galerkin method breaks space into segments called elements. Within each element, the value of the field is represented by the sum of n interpolating polynomials of order n, where n is the order of the element. There are $n + 1$ unevenly spaced nodes in the element, clustered toward the edges. At each node, exactly one of the interpolating polynomials takes on a value of one while the others are zero. An interpolating Lagrange polynomial has a functional form:

$$\ell_i(r) = \prod_{j=1, j \neq i}^{n} \frac{r - \xi_j}{\xi_i - \xi_j} \tag{2.10}$$

where ξ_i is a location of a node and where r is an arbitrary position [19].

Omitting the details of the derivation of this method, which can be found in Reference [19], the procedure for calculating the spatial derivative in one dimension is to first calculate the Legendre polynomials, rescaled by a factor depending upon their order. $\tilde{P}_n(r) = \frac{P_n(r)}{\sqrt{\gamma_n}}$ where $\gamma_n = \frac{2}{2n+1}$. The following procedure of differentiation and matrix inversion can be used to calculate the derivative matrix for each element, D_r [19].

$$V_{ij} = \tilde{P}_j(r_i) \tag{2.11}$$

$$V_{r,(i,j)} = \frac{d\tilde{P}_j}{dr}\Big|_{r_j} \tag{2.12}$$

$$V^T D_r^T = (V_r)^T \tag{2.13}$$

In practice, we use a custom package, the Template Numerical Toolkit (TNT) library and JAMA, to invert the equation using LU decomposition. Beware! TNT and JAMA are not thread safe, and cannot be used with shared memory parallelization. They result in race conditions, and it was ultimately necessary to rewrite the parallelized portion of the code to avoid the TNT classes.

The Discontinuous Galerkin method helps damp error introduced by discontinuities in

11

the field, provided they remain at element boundaries. We make use of this in our self-force calculations in the neighborhood of the particle, to be described in Chapter 5.4. The numerical flux is a way of accounting for the discontinuity in the flow between neighboring elements. There are multiple ways of calculating this flux, but in our code, we use a version relevant to linear hyperbolic problems, such as Equation 2.7, which, recall, is specialized to a one-dimensional problem. In this case, $A = S\Lambda S^{-1}$, for some transformation matrix S, where Λ is a diagonal matrix. Let Λ^+ and Λ^- be the positive and negative eigenvalues of Λ, respectively, corresponding to the outgoing and in-going waves. Then the numerical upwind flux is given by

$$(\hat{n}\dot{F}) = S(\Lambda^+ S^{-1}u^- + \Lambda^- S^{-1}u^+) \tag{2.14}$$

This flux, based upon the state vector interior to (u^-) and exterior to (u^+) the element, at each end of the element, is distributed across the whole element from end to end via the lift matrix [19].

2.2.2 Time evolution

Time evolution in our code is handled by a fourth order low storage Runga Kutta method. Instead of the standard fourth order Runga Kutta method, this method takes five sub-time-steps, but only the most recent sub-time-step needs to be stored.

$$p^{(0)} = u^n k^{(i)} = a_i k^{(i-1)} + \delta t RHS(p^{(i-1)}, t^n + c_i \delta t) p^{(i)} = p^{(i-1)} + b_i K^{(i)} u_h^{n+1} = p^{(5)} \tag{2.15}$$

Here steps two and three are repeated for $i = 1 - 5$, first k, then p, then increase i and repeat. The coefficients a_i, b_i, and c_i are given in Reference [19].

2.3 Wave equation on flat space-time

Using Gaussian initial conditions in ψ and setting the ρ initial conditions to the derivative of that Gaussian, I have produced the evolution shown in Figure 2.1. The Gaussian marches to the right over a number of time steps, hits the periodic boundary conditions,
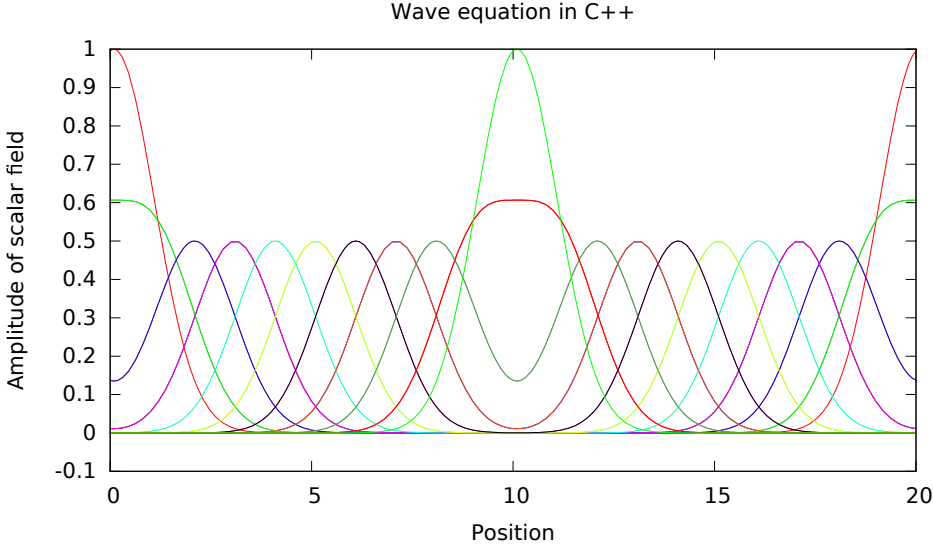
Figure 2.1: Waves evolving over time for Gaussian initial conditions

and re-enters the one-dimensional space on the left, eventually returning to its original position. A similar progression can be seen in Figure 2.2 for sinusoidal initial conditions.

The Discontinuous Galerkin method has truncation error that scales as h^{n+1}, where h is the element size and n is the polynomial order of the elements. The L_2 error is defined as the square root of the sum of the squared differences across all space, after one complete cycle of the system. The scaling of the L_2 error with DG order and with element size is shown in Figures 2.3 and 2.4. The scaling matches expectations until roundoff error is hit, where the error stops improving with order or smaller element size. Not shown, this same pattern was seen for the L_0 error, which is the maximum error over all space.
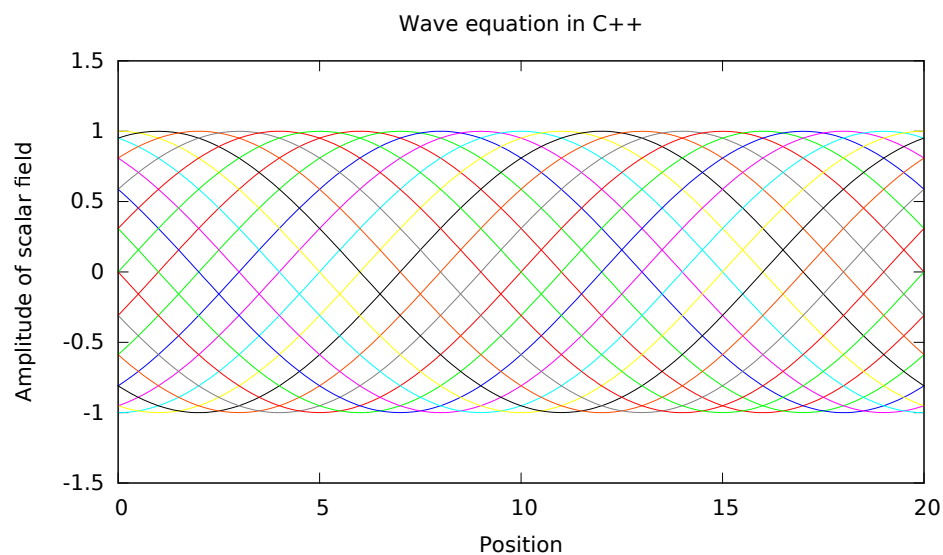
Figure 2.2: Waves evolving over time for sinusoidal initial conditions
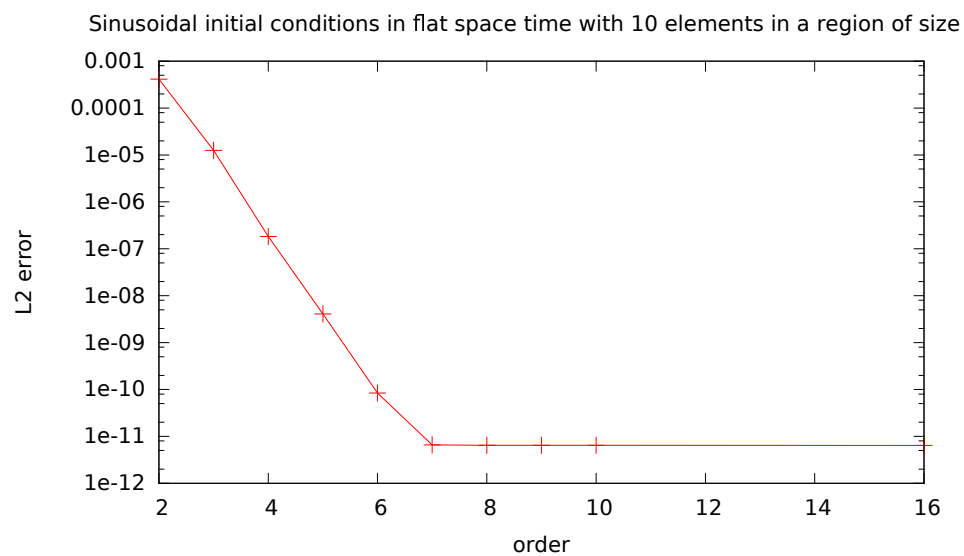
Figure 2.3: L_2 error scaling with DG order for sinusoidal initial conditions
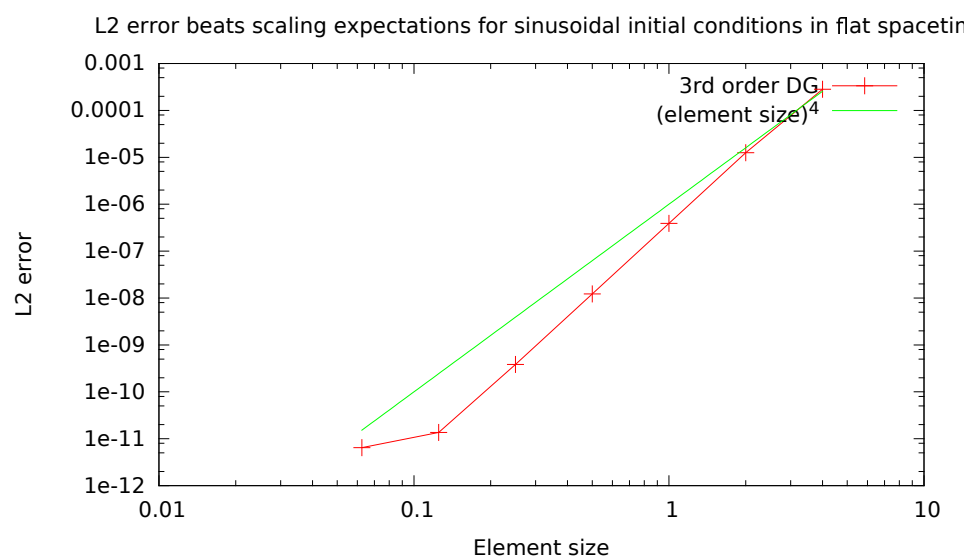
Figure 2.4: L_2 error scaling with element size for sinusoidal initial conditions

Chapter 3
A scalar field on a Schwarzschild background without a source

3.1 Scalar field on Schwarzschild space-time

Although the final goal in this field is to compute tensor waveforms that can be used as templates for LISA searches, for the purposes of obtaining the desired accuracy, it is important to improve our computational methods. We do this by performing comparison studies using scalar, rather than tensor, self force methods to make the problem more tractable. I have performed the simplest of such comparison studies– I have reimplemented Peter Diener's Fortran scalar self-force code, with a slightly modified design, in C++. The desired goal was for the results to match to within roundoff error. This was achieved for scalar fields without a source and for scalar fields with point sources on circular orbits (see Chapter 4.3.

3.1.1 Scalar field wave equations

A scalar field is a field that has one one degree of freedom at a given point in space– rather than being a matrix, it has a single value. The scalar wave equation, on a Schwarzschild background,in the absence of a source, is, in its most abstract form, the same as in flat space-time.

$$\Box\Psi = 0 \tag{3.1}$$

The details of the implementation are a little different, to account for the curvature of space. This enters through the metric. For a scalar field, the D'Alembertian can be written

$$\Box\Psi = \frac{1}{\sqrt{-g}}\partial_\mu(\sqrt{-g}\partial^\mu\Psi) = 0 \tag{3.2}$$

where g is the determinant of $g^{\mu\nu}$. [55]

- **Multipole moment decomposition**

In our approach, spherical harmonics are used to reduce the three spatial dimensions to a one dimensional problem, in terms of the radius and a sum of an infinite number of discrete spherical harmonic modes, characterized by numbers l and m, where l ranges from 0 to ∞ and m ranges from $-l$ to $+l$ for each l [**?**]. The field is written as

$$\Psi = \sum_{l,m} \Psi^{lm}(t,r) Y^{lm}(\theta,\phi) \tag{3.3}$$

This separation of variables ansatz can be used to simplify the wave equation in any coordinate system, since the angular coordinates are not transformed in any of the coordinate systems we use. We make use of the identity

$$r^2 \nabla^2_{\theta,\phi} Y^{lm} = -l(l+1) Y^{lm} \tag{3.4}$$

where $\nabla^2_{\theta,\phi}$ is the angular part of the Laplacian, which has a $\frac{1}{r^2}$ dependence. This introduces a term proportional to $l(l+1)\Psi^{lm}(t,r)$ for each l, m.

- **Tortoise coordinates**

In this code, we use a mixture of tortoise (Eddington-Finkelstein) and hyperboloidal coordinates. Tortoise coordinates have the property that they go to infinity at the horizon (scri minus) and infinity at light-like infinity (scri plus). It is beneficial to place scri minus at an unreachable distance in coordinate space so that the boundary conditions at the horizon become trivial and there is no leakage of information from the interior of the black hole to outside the horizon in the process of discretization. It is also beneficial to increase the number of computational elements near the horizon by compactifying the coordinates there. Tortoise coordinates transform only the radial coordinate, leaving the angular and

time coordinates alone. [55]

$$t_* = t \tag{3.5}$$

$$r_* = r + 2GM \ln \left| \frac{r}{2GM} - 1 \right| \tag{3.6}$$

$$\theta_* = \theta \tag{3.7}$$

$$\phi_* = \phi \tag{3.8}$$

We solve the wave equation in tortoise coordinates in one region of the code. I have re-derived this equation in Mathematica and verified the form that appears in Peter Diener's Fortran scalar self-force code. The wave equation in tortoise coordinates is

$$\frac{d^2\psi}{dt^2} = \frac{d^2\psi}{dr_*^2} - \frac{1}{r^5}\left(\frac{2M}{r} + (l+1)l\right)\left(1 - \frac{2M}{r}\right)\psi \tag{3.9}$$

r is in Schwarzschild coordinates, r_* is in tortoise coordinates, l is the spherical harmonic l-mode (discussed below), which accounts for the angular dependence, and ψ is a function of tortoise coordinates.

- **Hyperboloidal coordinates**

    Hyperboloidal coordinates are necessary; however, because infinities are computationally unreachable. It is clear that space infinitesimally close to the horizon is important, since the curvature of space is strongest there, and it is still causally connected to the exterior region. To make the horizon reachable in a finite number of computational elements, while retaining the property that more computational elements are placed near the horizon than far away, hyperboloidal coordinates are introduced in the region closest to the horizon. In a middle region, tortoise coordinates are used. In the region furthest from the black hole, hyperboloidal coordinates are used again to place scri plus at a finite number, yet maintaining the property that fewer computational elements are needed far away from the black hole. Hyperboloidal coordinates are described by the transformation [4]

18

There are a few key features. The angular coordinates are not transformed. The time coordinate preserves the stationarity of the background metric, and thus the new time variable, τ, must be related to the old time variable, t_*, by an offset dependent only upon r_*, $\tau = t - h(r_*)$. For in-going waves in the inner region, $t - r_* = \tau - \rho$ and in the outgoing region, $t + r_* = \tau + \rho$ to preserve the structure of the light cone. Bernuzzi, Nagar, and Zenginoglu define $H = \frac{dh}{dr_*}$. They introduce a compactification that depends on a window function Ω [60], such that the tortoise radius gets redefined $r_* = \frac{\rho}{\Omega(\rho)}$, resulting in an expression for the height function H in terms of the hyperboloidal radius, $H(\rho) = 1 - \frac{\Omega^2}{\Omega - \rho \Omega'}$. Their final wave equation, for in-going waves, is [4]

$$\partial_t^2 - \partial_{r_*}^2 = -(1 - H^2)\partial_\tau^2$$
$$+(1 - H)(-2H\partial_\tau\partial_\rho + (1 - H)\partial_\rho^2 - (\partial_\rho H)(\partial_\tau + \partial_\rho)) \qquad (3.10)$$

I have verified this equation, and derived the outgoing wave equation, in Mathematica.

- **Initial conditions and boundary conditions**

  Since there is no source for the scalar field in the C++ code, it must be set to some initial value and allowed to fall into the black hole or radiate away its energy to infinity. A Gaussian initial condition in the time derivative of the scalar field, centered at computational coordinate zero (which was some physical distance outside the black hole horizon), was chosen. Initial conditions and the first time-step are shown in Figures **??**.

  Boundary conditions were matched automatically by the coordinate transformation between tortoise and hyperboloidal layers. At scri minus and scri plus, the boundary conditions were that the scalar field be set to zero.

3.2 Theoretical expectations

The phase without a source is like the ring-down phase of the system. There are two analytically predicted behaviors that characterize the ring-down phase. After the plunge from the innermost stable circular orbit, quasi-normal mode ringing begins. Eventually
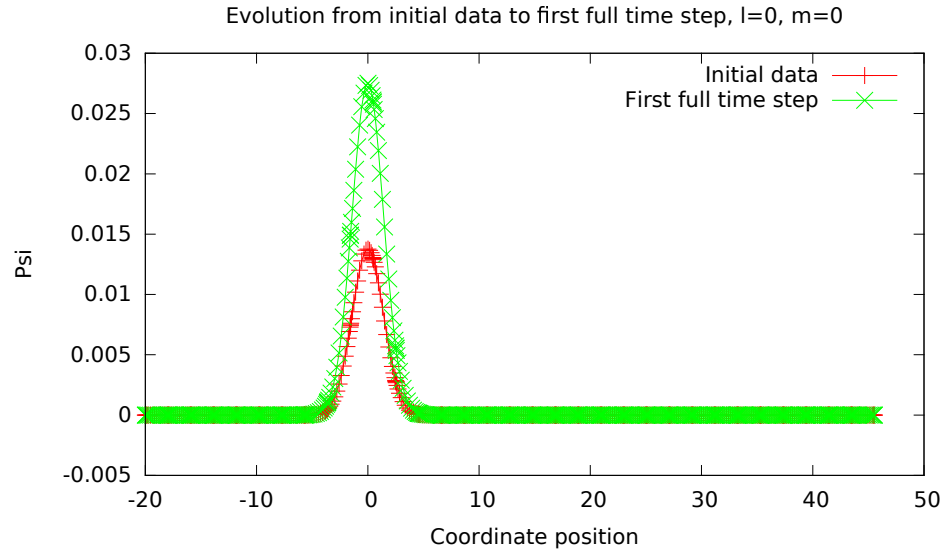
Figure 3.1: Scalar field spatial slice initial condition and first full time-step for l=0.
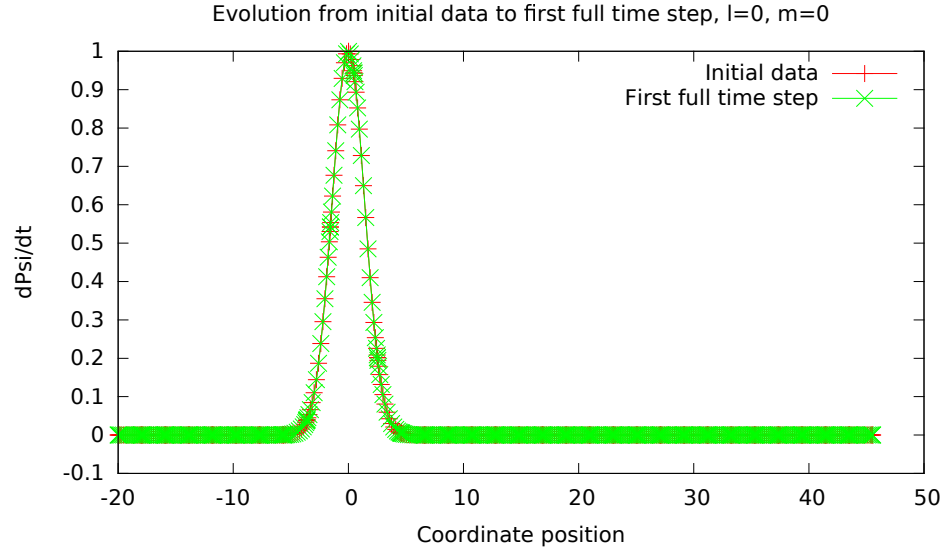
Figure 3.2: Time derivative of the scalar field spatial slice initial condition and first full time-step for l=0.
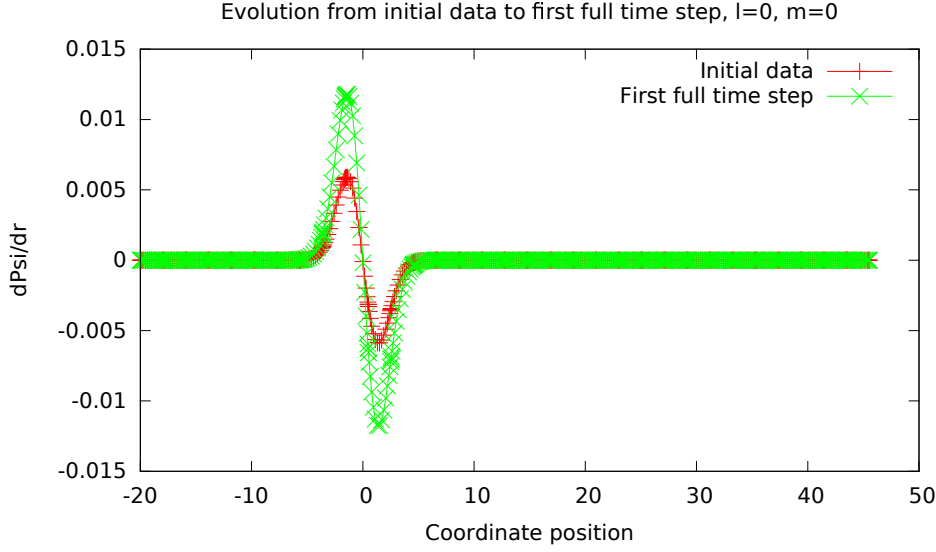
Figure 3.3: Radial derivative of the scalar field spatial slice initial condition and first full time-step for l=0.

that fades into a long, power law tail.

3.2.1 Quasi-normal modes

A field, such as a scalar or tensor field surrounding a black-hole, exhibits quasi-normal mode ringing as it relaxes into or away from the black hole. Hence, in LIGO, the first overtone of the first fundamental quasi-normal mode was seen after the merger phase during the ring-down phase in LIGO's first detection [28]. In EMRI's, quasi-normal modes are expected to be detected by LISA after the small black hole crosses the large black hole's horizon, following the plunge from the innermost stable circular orbit. The same set of quasi-normal modes is expected for any tensor field perturbed around a black hole, regardless of why, as long as there is no ongoing source present. The case is very similar with scalar fields, though the spectrum of quasi-normal modes is slightly different.

A quasi-normal mode decays at a nearly stably frequency and a nearly steady exponential decay rate, with slight changes due to the loss of energy from the system. These rates have been calculated by Reference [5] and made available online. I have used their theoretical expectations for the first overtone at each l and m mode to fit my simulation data in Figures [?] and [?]. Notice that for higher m, the quasi-normal mode frequency is

21
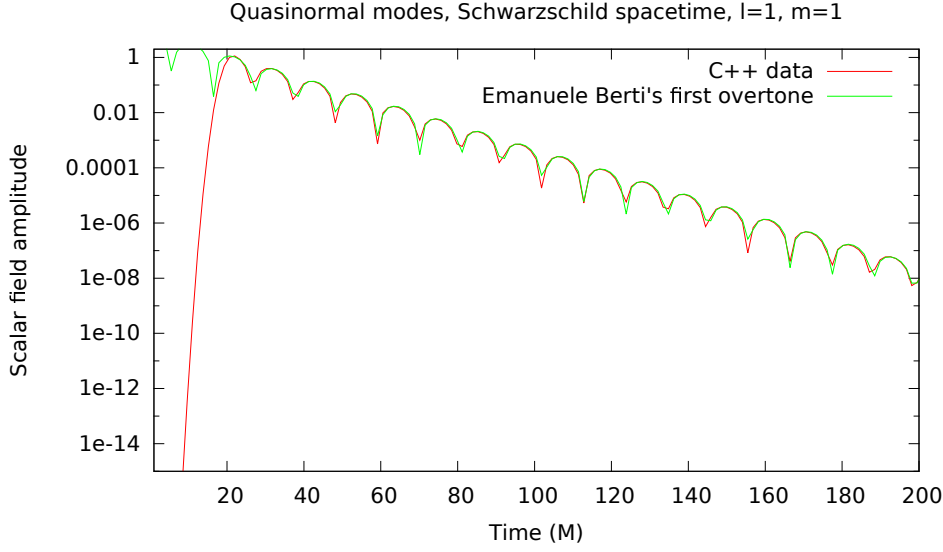
Figure 3.4: Quasi-normal mode for l=1,m=1

higher and the decay is faster.

3.2.2 Power law tails

After quasi-normal mode ringing settles down, power law tails begin. Both are due to backscattering of the waves off the background metric, but they take place in different regimes of time that has elapsed relative to perturbation initial conditions and background black hole mass. In 1972, Richard Price predicted that the tails would scale as $t^-(2l+2)$ or $t^-(2l+3)$ depending on initial conditions [46]. In our choice of initial conditions, $t^-(2l+2)$ matches best for the choices of l explored. Figure 3.6 shows a mode for which I successfully recovered a power law tail. Figure 3.7 demonstrates that truncation error may dominate at high l, and that it may be necessary to increase the DG order to resolve all l-modes in a simulation.
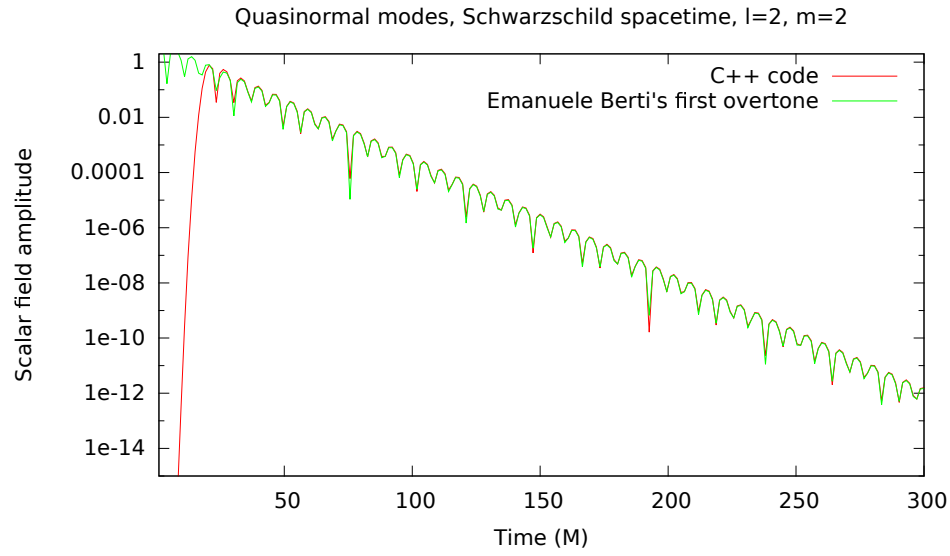
Figure 3.5: Quasi-normal mode for l=2, m=2
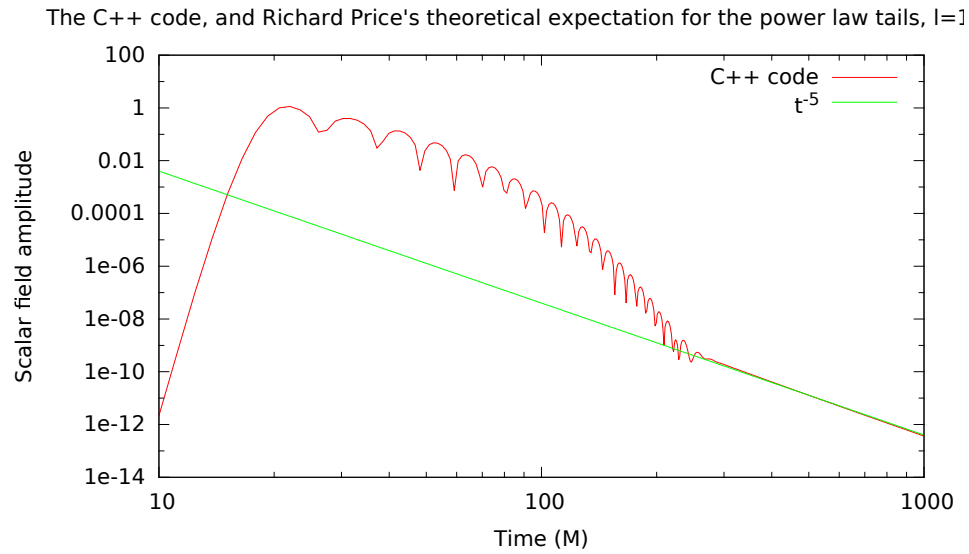
Figure 3.6: Power law tail, l=1, m=1
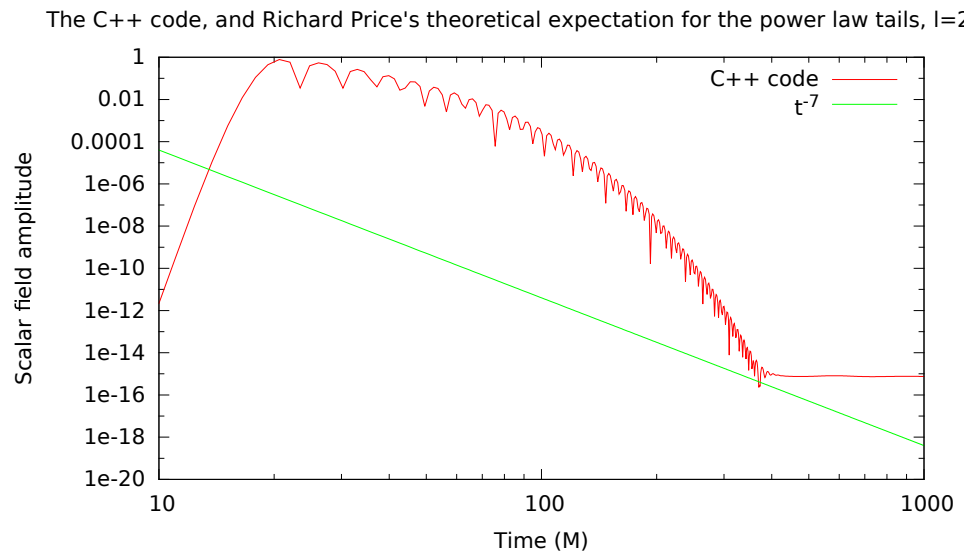
Figure 3.7: Power law tail does not match expectations due to truncation error in DG method, l=2, m=2

Chapter 4
Circular orbits on a Schwarzschild spacetime

4.1 Self Force

A test particle orbiting a black hole follows a geodesic, which is the path of extremal proper time. This is described by the geodesic equation,

$$\frac{d^2 x^\mu}{d\tau^2} + \Gamma^\mu_{\rho\sigma} \frac{dx^\rho}{d\tau} \frac{dx^\sigma}{d\tau} = 0 \tag{4.1}$$

where τ is the proper time and $\Gamma^\mu_{\rho\sigma}$ is the Christoffel symbol, given by [6]

$$\Gamma^\sigma_{\mu\nu} = \frac{1}{2} g^{\sigma\rho} (\partial_\mu g_{\nu\rho} + \partial_\nu g_{\rho\mu} - \partial_\rho g_{\mu\nu}) \tag{4.2}$$

However, a black hole, of any size, is not a test particle. In the limit of an EMRI, the additional force can be treated perturbatively in the mass ratio of the two particles, in the relativistic case. In the scalar case, the self force is simply written as a delta function source to the wave equation dependent upon the particle's position in time [56]

$$\Box \Psi^{ret} = -4\pi q \int \delta_4(x, z(\tau')) d\tau' \tag{4.3}$$

In this equation, $\Box$ is the D'Alembertian and $z(\tau')$ is the evolving path of the source in space-time as a function of the particle's proper time. The retarded field Ψ^{ret}, is defined to be the field determined by physics taking place at $t_r = t - \frac{|\vec{r} - \vec{r}'|}{c}$; that is, at some distance away from the particle's path, the physical effects of gravity on the scalar field are retarded by light travel time. In the scalar approximation, the particle acts as a delta function point source, with a charge of q and mass m. That charge may accelerate or evolve with time; see chapter 8.2.2.
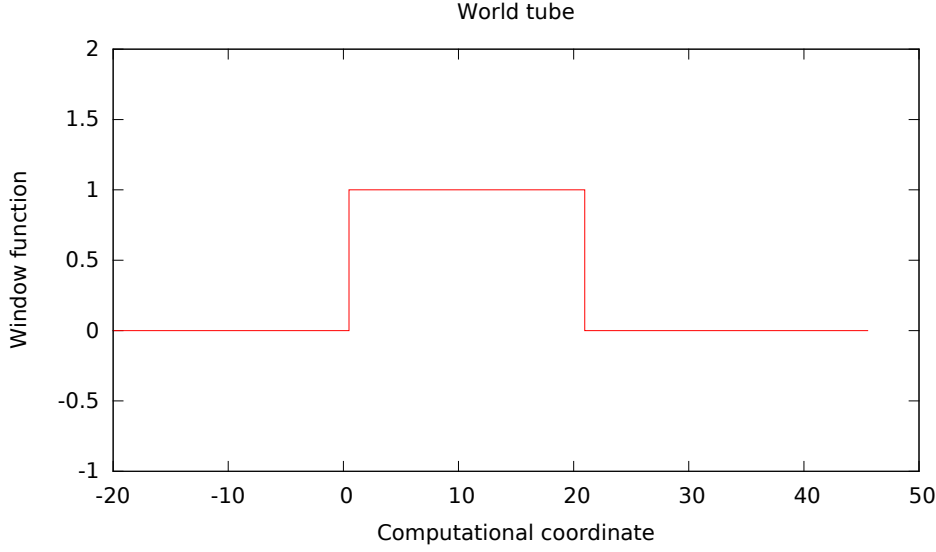
Figure 4.1: Spatial slice of the world tube window function.

The retarded field is singular at the location of the particle due to the delta function source. Singularities are computationally problematic. To regularize this singularity, a regular field is created through the use of an effective source.

$$\Psi^R = \Psi^{ret} - \Psi^S \tag{4.4}$$

$$\Box\Psi^R = S_{eff} \tag{4.5}$$

$$S_{eff} = q\delta(x, x_0) - \Box(W\Psi^S) \tag{4.6}$$

$$F_\alpha = (\nabla_\alpha \Psi^r)|_{x=x_0} \tag{4.7}$$

The regularized field, Ψ^R, is defined in terms of the retarded field with the singular field, Ψ^S, subtracted. This leads to the definition of an effective source, S_{eff}, that is zero inside the neighborhood of the particle, due to the world tube window function around the particle, shown in Figure 4.1, and that approximates the source outside that region. Outside that region, the regularized field is equal to the retarded field. The self-force can be derived from the final equation given above, F_α is merely a gradient of the field itself [?].

26

4.2 World tube

The world tube window function around the particle carves out a ring around the black hole in the orbital plane, due to the use of spherical harmonics to increase the dimensionality of space. In my C++ code, the world tube extends throughout the entire tortoise region, ending at the transitions to the hyperboloidal regions. When calculating numerical fluxes at this boundary, it is necessary to account for both the coordinate transformations between either side of the boundary and the transformation between regular and retarded field.

While on a circular orbit, the particle follows a fixed path that prevents it from inspiraling. This does not conserve energy, since energy is radiated away into the black hole and to infinity by the scalar waves. Clearly, we are artificially inputting energy into the simulation by holding the particle fixed on its orbit. This, in a nutshell, explains the need for scalar (or gravitational) radiation, and for self force in this limit.

4.3 Comparison between C++ and Fortran codes

I've performed extensive comparisons between Peter Diener's Fortran code **??**, implementing the same thing, and my C++ code. To roundoff precision, they agree, as evidenced by the near-machine-precision (10^{-15}) levels of agreement in both absolute and relative error that I achieve in Figures 4.2, 4.3, 4.4, and 4.5
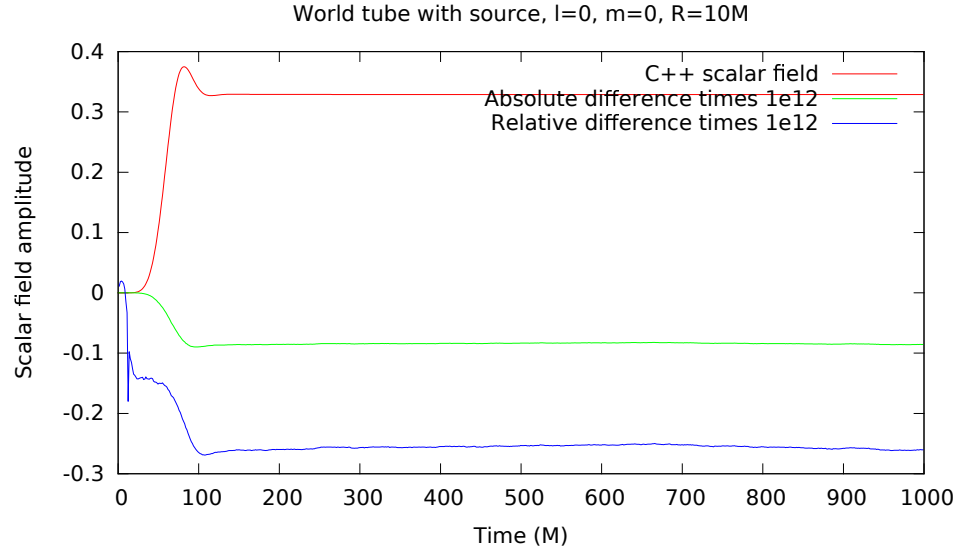
Figure 4.2: Comparison between Fortran and C++ codes for a particle on a circular orbit, l=0, m=0.
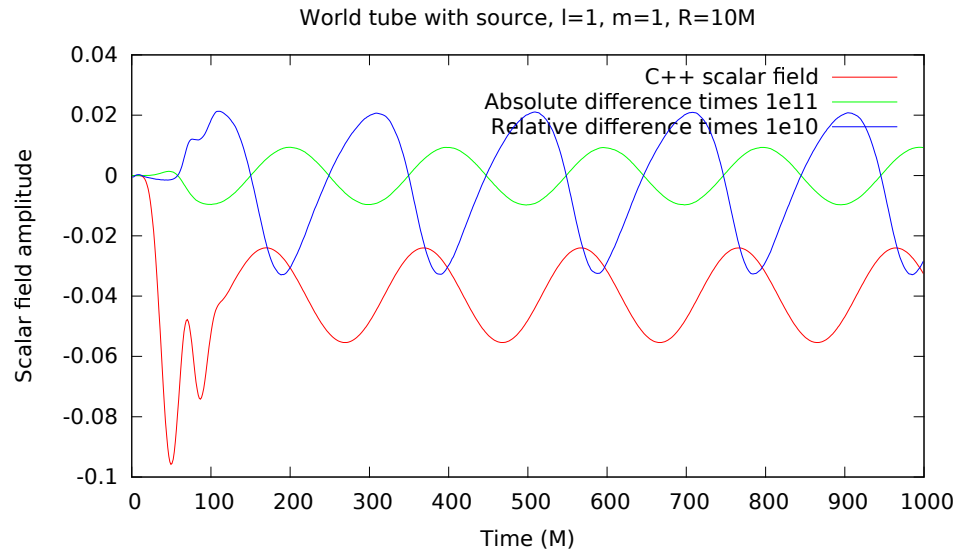
Figure 4.3: Comparison between Fortran and C++ codes for a particle on a circular orbit, l=1, m=1.
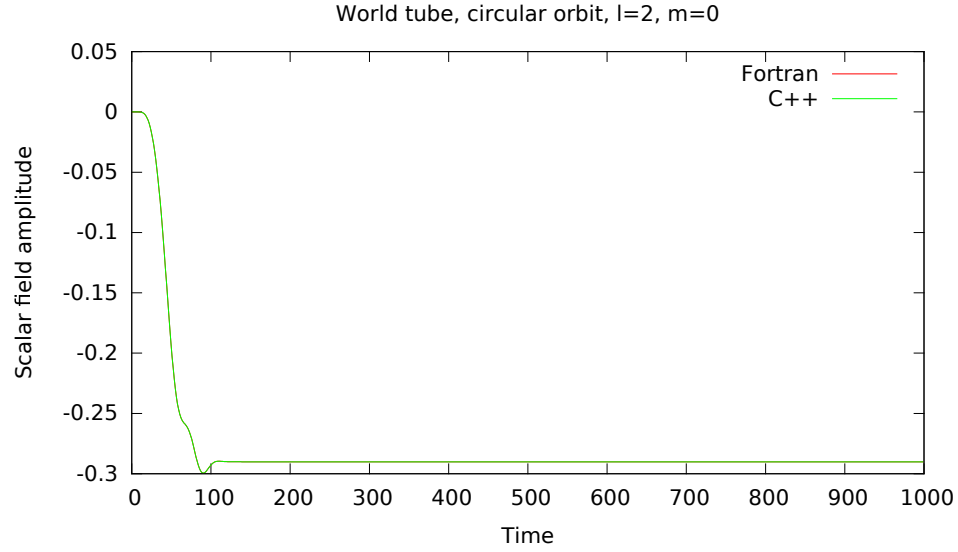
Figure 4.4: Comparison between Fortran and C++ codes for a particle on a circular orbit, l=2, m=0.
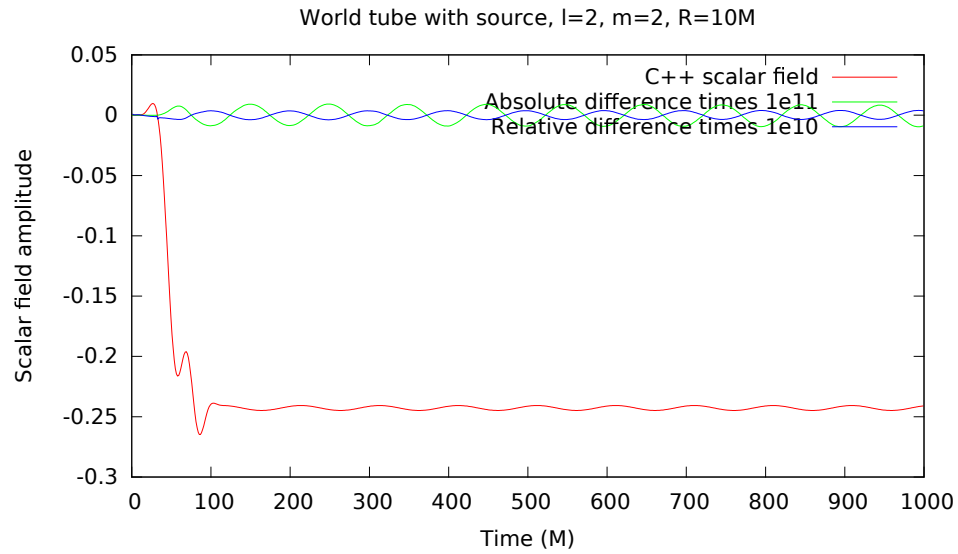
Figure 4.5: Comparison between Fortran and C++ codes for a particle on a circular orbit, l=2, m=2.

Chapter 5
Eccentric orbits on a Schwarzschild spacetime

For eccentric orbits, there are two primary additional physical or computational effects to consider. One is the need for eccentric orbit parameters, expressed in terms of an eccentricity and a semilatus rectum, determined by an energy and an angular momentum. The second is the addition of a time dependent coordinate transformation region between tortoise layers in the middle of the computational grid, containing the position of the particle for all times. In this section, I describe Peter Diener's Fortran code, using Niels Warburton's exact initial conditions for l-modes 0 through 5, and Barry Wardell's effective source, which I have run to produce eccentric orbit output. Similar computations have been done before, using the Discontinuous Galerkin method, by Reference **??**, for the gravitational tensor field case; however, the scalar Discontinuous Galerkin case is not yet published.

5.1   Orbital parameters

The orbital parameters of an eccentric orbit in a Schwarzschild space-time are defined through the following conditions.

$$E^2 = \frac{(p-2-2e)(p-2+2e)}{p(p-3-e^2)} \tag{5.1}$$

$$L^2 = \frac{p^2 M^2}{p-3-e^2} \tag{5.2}$$

Here, E is the energy and L is the angular momentum. e is the eccentricity and p is the semilatus rectum, which is a dimensionless measure of half the "width" of the eccentric orbit. More clearly, $r_{periastron} = \frac{pM}{1+e}$ and $r_{apastron} = \frac{pM}{1-e}$. χ is a parameter that runs from 0 to 2π in one radial cycle (as opposed to ϕ, which runs from 0 to 2π in one angular cycle).

In terms of these parameters [44],

$$r'(\chi) = \frac{pMe\sin(\chi - w)}{[1 - e\cos(\chi - w)]^2} \tag{5.3}$$

$$\phi'(\chi) = \sqrt{\frac{p}{p - 6 - 2e\cos\nu}} \tag{5.4}$$

$$t'(\chi) = \frac{p^2 M}{(p - 2 - 2e\cos\nu)(1 + e\cos\nu)^2}$$

$$\frac{d\chi}{dt} = \left(\frac{dt}{d\chi}\right)^{-1} \tag{5.5}$$

where $\nu = \chi - w$. For an eccentric orbit, χ and ϕ are evolved using a fourth order Runga Kutta integration using the oscillating orbits framework described in Reference **??**. For a self consistent evolving orbit with the back-reaction effect of the self-force, see future work in Chapter 8.2.2.

5.2   Time dependent coordinate transformation

In the case of an eccentric orbit, it is necessary to ensure that the particle always remains within the tortoise region, so that the effective source remains valid. We use a time dependent coordinate transformation to keep the particle fixed at a specific coordinate location while the space in its immediate neighborhood evolves. With the proper boundary conditions, enforced by the numeric flux, this simulates a particle on an eccentric orbit and produces the same self-force and the same scalar waves at scri plus. The necessary time dependent coordinate transformation can be found in Reference [12]. It transforms from tortoise coordinates, ξ, to time dependent coordinates, x. The location of the particle $\xi_p(t)$, varies in tortoise coordinates but is fixed in time dependent coordinates (x_p). a and b are the boundaries of the time dependent region, in computational coordinates.

$$x = a + \frac{x_p - a}{\xi_p - a}(\xi - a) + \frac{(b - \xi_p)(\xi_p - a) - (x_p - a)(b - \xi_p)}{(\xi_p - a)(b - \xi_p)(b - a)}(\xi - a)(\xi - \xi_p) \tag{5.6}$$

I have used Mathematica to confirm the time dependent coordinate wave equation used in Peter Diener's Fortran scalar self-force code. Its time and radial components are

$$
\frac{d^2\psi}{dt^2} = \left(\frac{dx}{d\xi}\right)^{-3}\left[\frac{d^2x}{d\xi^2} - \frac{d^2x}{d\xi^2}\left(\frac{dx}{dt}\right)^2 - 2\frac{d^2x}{d\xi dt}\frac{dx}{d\xi} - \left(\frac{d^2x}{dt^2}\right)^2\right]\frac{d\psi}{d\xi}
$$
$$
+\left[-1 + \left(\frac{dx}{dt}\right)^2\right]\left(\frac{dx}{d\xi}\right)^{-2}\frac{d^2\psi}{d\xi^2}
$$
$$
-2\frac{dx}{dt}\left(\frac{dx}{d\xi}\right)^{-1}\frac{d^2\psi}{d\xi dt} \tag{5.7}
$$

It is necessary to invert the time dependent transformation and subtract the singular field from the scalar field (and its derivatives) to obtain in-going fluxes at elements just outside the world tube. Similarly, to obtain in-going fluxes inside the world tube, we must transform to time dependent coordinates and subtract the singular field from the scalar field. For outgoing fluxes, addition and subtraction are reversed.

5.3 Orbits

I have computed four orbits of the system, at DG order 44. Figure 5.1 shows the radius in Schwarzschild coordinates as a function of time. Figure 5.2 shows the sense in which this orbit is eccentric– if it did not precess, it would form an ellipse. Figure 5.3 depicts the physical path of the orbit, including precession. Figure 5.4 demonstrates why precession must exist. The periods of the angular variable ϕ and the parameter that governs the rate of radial evolution, χ, are not synchronized.

5.4 Self force output

The radial self-force is defined as $q\nabla^\alpha\Psi^R$ [?]. To compute this self force, it is necessary to sum over all l and m modes. In principle it is necessary to sum to $l = \infty$. Figures 5.5, 5.6, and 5.7 are computed using a fit to extrapolate to infinite l, based on an analytic sum of the remaining terms after the highest l-mode computed. See Chapter ?? for details of the mode sum. Two terms of the sum described in that chapter were used in the fit.
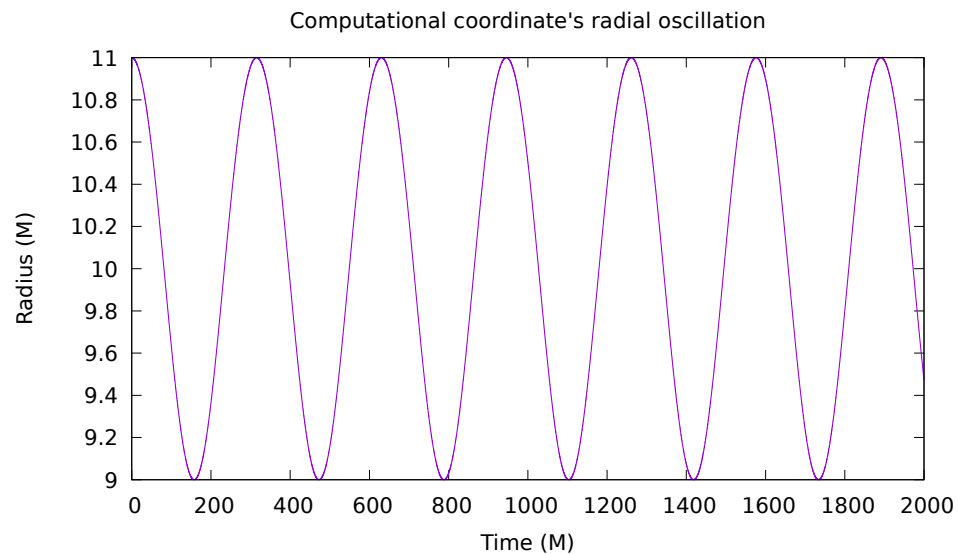
Figure 5.1: Schwarzschild r as a function of time over several orbits.
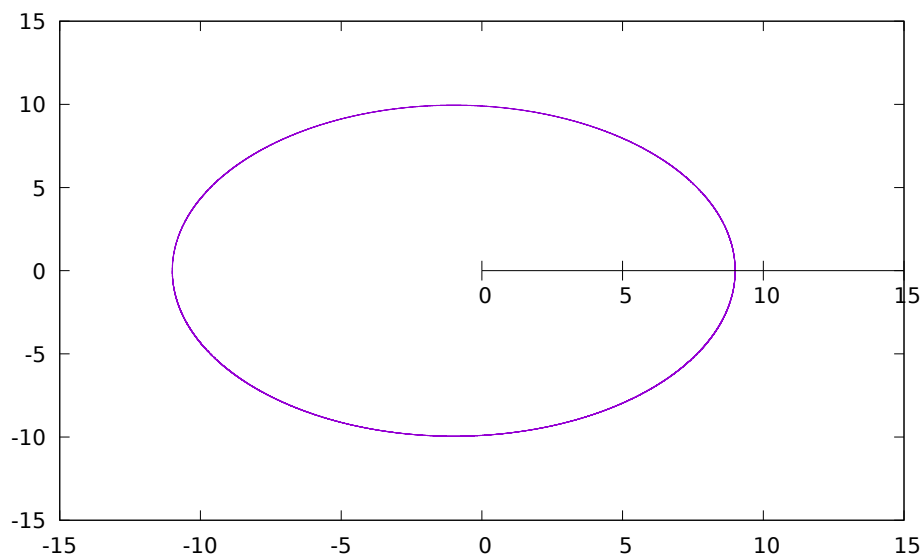
Figure 5.2: With χ as the angle in polar coordinates, the orbit forms an exact ellipse. This is the definition of χ, provided r is in Schwarzschild coordinates. Shown for $p = 9.9$ and $e = 0.1$, DG order 44
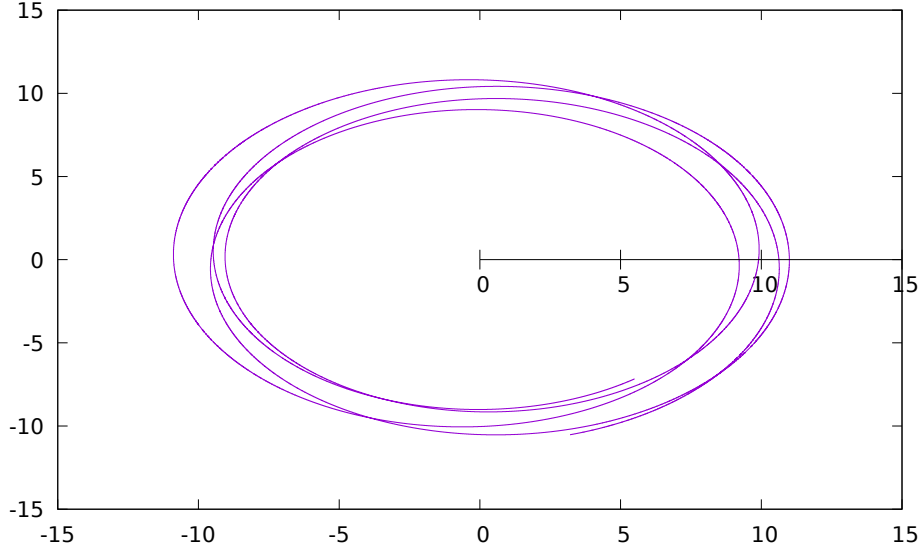
Figure 5.3: The orbit as it physically would exist, using Schwarzschild ϕ as the polar coordinate angle. The orbit precesses but does not inspiral since there is no generic evolution. Shown for $p = 9.9$ and $e = 0.1$, DG order 44
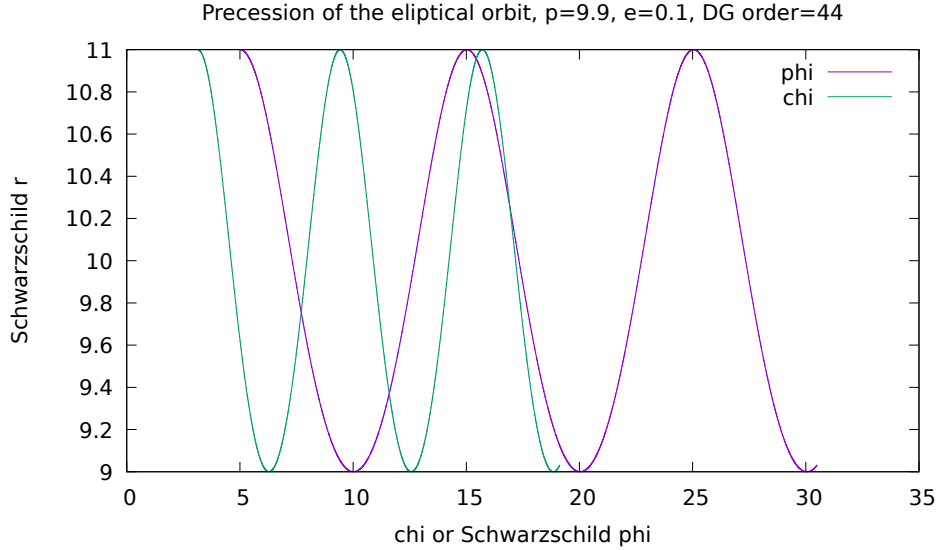
Figure 5.4: Precession of the eccentric orbit is demonstrated due to the inequality in the period of the angular variables χ, which represents the period of the radial oscillations, and ϕ, which represents the period of the angular oscillations. $p = 9.9$, $e = 0.1$, DG order 44.
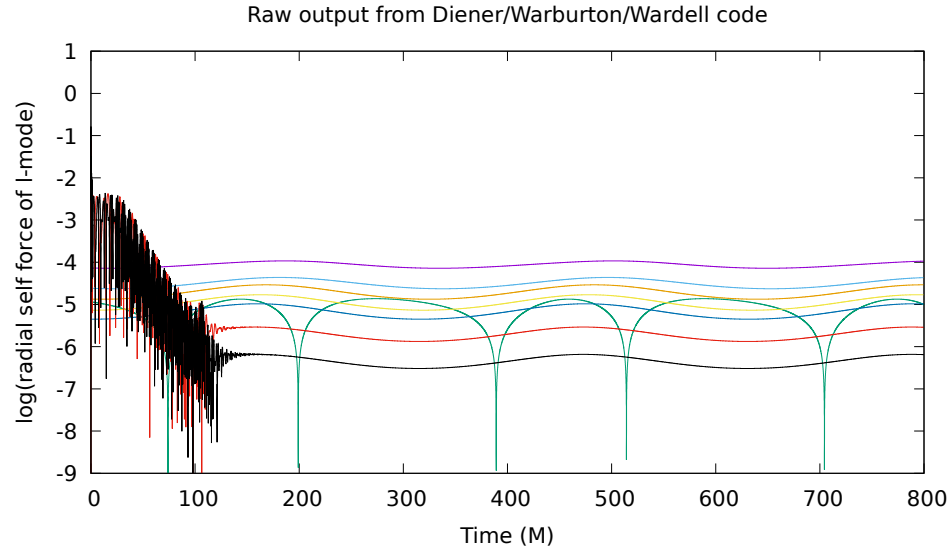
Figure 5.5: Raw output of Diener, Warburton, and Wardell code for DG order 44. Radial self force.
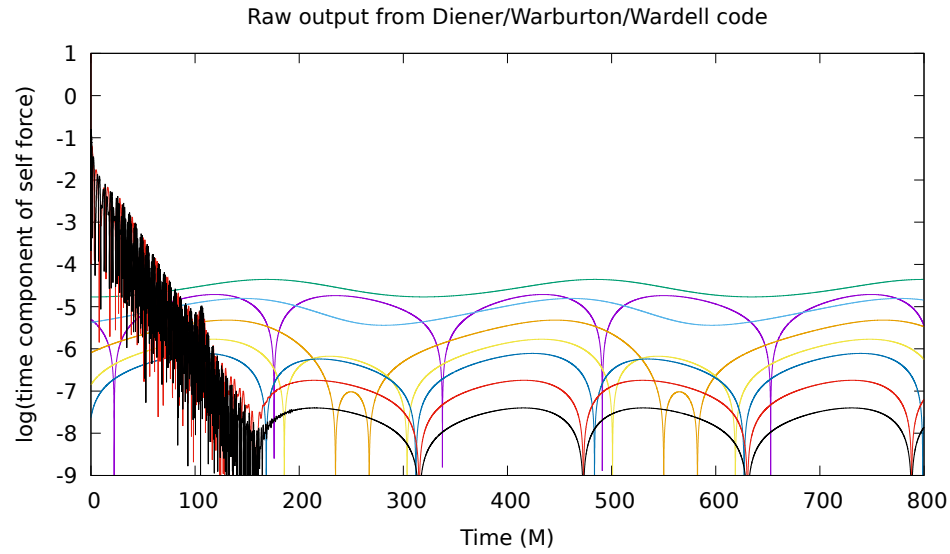
Figure 5.6: Raw output of Diener, Warburton, and Wardell code for DG order 44. Time component of the self force.
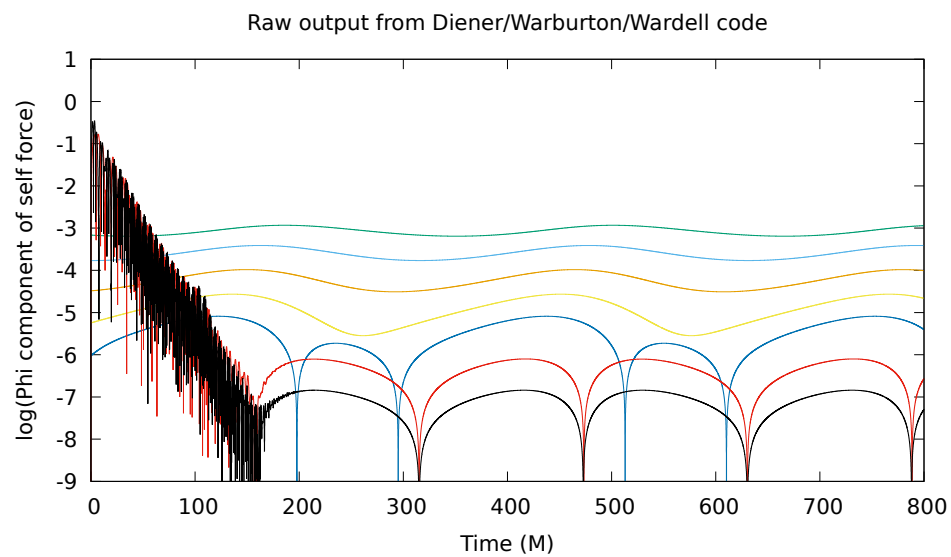
Figure 5.7: Raw output of Diener, Warburton, and Wardell code for DG order 44. Phi component of the self force.

Chapter 6
Extrapolating the self force to infinite Discontinuous Galerkin order

The Discontinuous Galerkin method results in truncation error that scales as h^{N+1}, where h is the element size and N is the order of the interpolating polynomials within the element. [19] The radial self force is given by the radial derivative of the scalar field, $F_r = \partial_r \Psi$. However, to obtain this quantity, it is necessary to sum the radial derivatives over all l and m modes. Let $F_l = \sum_{m=-l}^{l} F_{lm}$. Each of these modes, separately, follows the DG convergence scaling laws. It should be possible to extrapolate to infinite DG order based and obtain F_{inf}, the self force for a given l-mode at infinite DG order.

The Lagrange interpolating polynomials that are used as the basis for the Discontinuous Galerkin method may also be used for extrapolation. Consider the case of a three degrees of freedom, for a quadratic polynomial. If $y_i = f(x_i)$ for $i = 0 - 2$ [45],

$$
\begin{aligned}
P(x) = \quad & \frac{(x-x_1)(x-x_2)}{(x_0-x_1)(x_0-x_2)} y_0 \\
& + \frac{(x-x_0)(x-x_2)}{(x_1-x_0)(x_1-x_2)} y_1 \\
& + \frac{(x-x_0)(x-x_1)}{(x_2-x_0)(x_2-x_1)} y_2
\end{aligned}
\tag{6.1}
$$

However, this form of extrapolation is insufficient for the case of a function that is fundamentally exponential in form. Nowhere does it approximate a polynomial. It is necessary to extend the extrapolation to one based upon exponential, rather than polynomial, assumptions about the underlying functional form.

The three-point exponential extrapolation is motivated by our assumption that Discontinuous Galerkin error is one-sided in the truncation error regime– it is not random; hence, the self force more or less monotonically approaches a limit. In the round-off error regime where the error is random, the self-force is no longer monotonically decaying. As long as it

is monotonically decaying, it can be written in the form of $F_r(n,l) = F_\infty(l) + c(l)\exp[-\alpha n]$, where n is the DG order. For a given mode, the three-point extrapolation is given by

$$h = \frac{F_r(n_1,l) - F_r(n_2,l)}{F_r(n_1,l) - F_r(n_3,l)} \tag{6.2}$$

$$g(\alpha) = \frac{\exp[\alpha(n_1-n_2)]-1}{-1+\exp[\alpha(n_1-n_3)]} \tag{6.3}$$

$$g(\alpha) - h = 0 \tag{6.4}$$

$$c(l) = \frac{F_r(n_1) - F_r(n_2)}{\exp[-\alpha n_1] - \exp[-\alpha n_2]} \tag{6.5}$$

$$F_\infty(l) = F_r(n_3) - c(l)\exp[-\alpha n_3] \tag{6.6}$$

This technique of extrapolating from various resolutions to produce a correction to the error is known as Richardson extrapolation, and can be done in finite difference schemes, Runga Kutta schemes, and other numerical schemes as well. In the middle step, it is necessary to use the bisection method for root finding, numerically, with the condition that α may never be less than zero since the solution must decay. If the three points are not monotonic, sometimes there is not a solution. I use extrapolation starting orders from the set 12, 16, 20, 24, 28, 32, and 36, with additional data at orders 40 and 44 that may be used as points two and three in the extrapolation. In order to use data from several different DG orders, it was necessary to interpolate between the times at which each order was computed to some desired common set of times, since each order takes a different time that decreases with increasing order so that the grid remains space-like within a full Runga Kutta time-step. Figure 6.1 shows the form of $g(\alpha)$. From this plot, it is clear why h must be greater than 0.5 in order for $g(\alpha) - h$ to have a root.

Since some modes fail, it is not possible to chose the same starting order for the extrapolation for all modes and all times. The first attempt I made to improve the choice of starting order was to chose the highest starting order for which no lower starting order had been unsolvable. Figure 6.2 shows this approach leads to some discontinuities in the time evolution of F_∞ in some l-modes ($l = 3$ is shown).
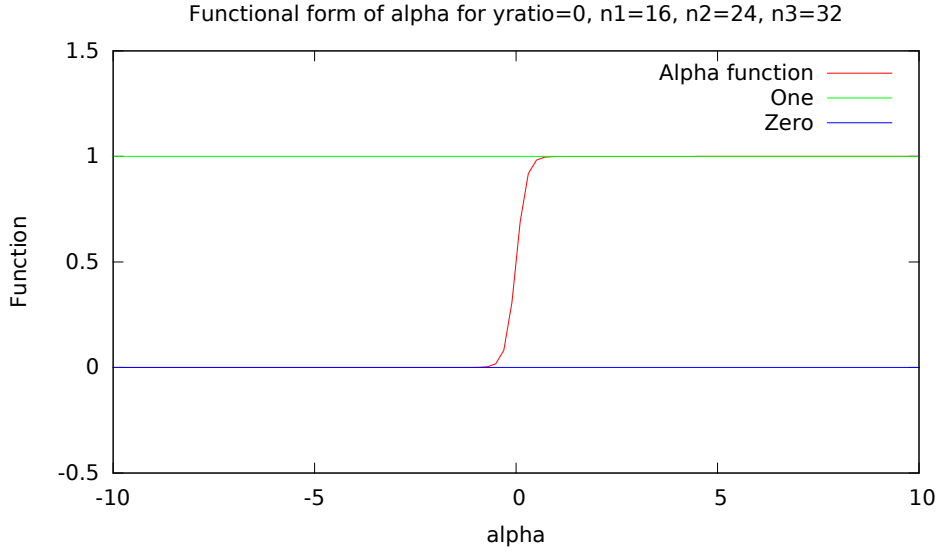
Figure 6.1: $g(\alpha)$, h must be greater than 0.5 for the mode and starting order to have a solution at that specific time.
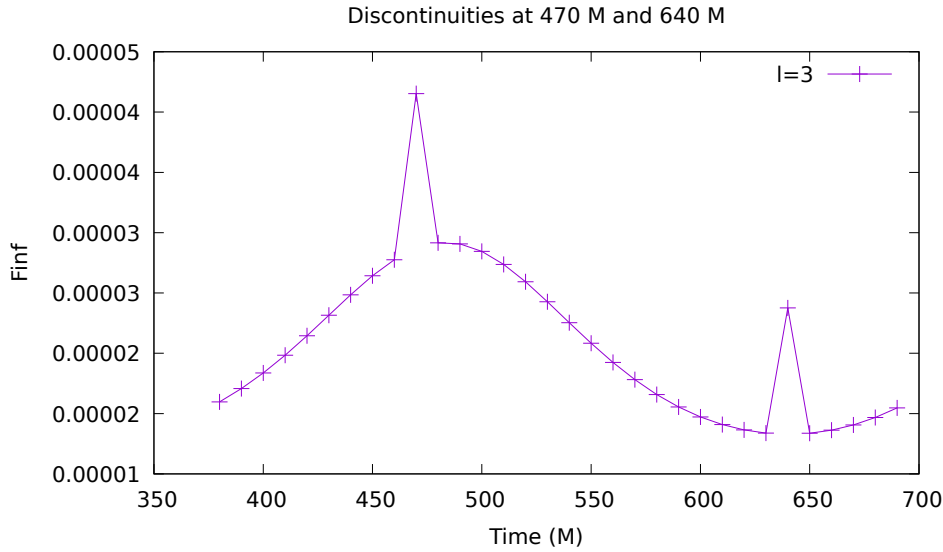
Figure 6.2: Starting order was chosen by iterating from the lowest order to the first order for which the "mode failed", and choosing the maximum starting order that succeeded. When F_{inf} is evolved over one full orbital cycle, some l-modes shows discontinuities at some times. l=3

Starting Order	F_∞
0	no solution
1	2.40975299617e-05
2	2.40975300465e-05
3	2.40975300114e-05
4	no solution
5	2.40975299291e-05
6	2.40975299148e-05

Table 6.1: Manual starting indices and F_{inf} values for t=632, l=2.

To address this concern, I examined the choice of starting order more closely for specific times where discontinuities were present. One example, for $l = 2$ and $t = 632M$, is shown in a Table 6.1. Figure 6.3 shows an example where no solution is found. The roundoff noise is visible in Figure 6.4 at high DG orders. In Figure 6.5, it is possible the effect at high DG orders is roundoff noise in the $F_r(n, l)$ values of the points, but it is more likely that it is roundoff noise in the choice of F_∞ due to limitations of the root finding method, resulting in an incorrect offset of the curve. Figure 6.6 shows that after selecting an average of the reasonably similar values from Table 6.1, the discontinuity in the $l = 2$ $t = 632M$ radial self-force becomes smooth.

6.0.1 Checking for discontinuities in F_{inf} for each each l-mode

In the median approach, the starting orders that had a solution at each time and for each mode are ordered by their F_{inf} values. The median value of F_{inf} is selected, presumably discarding those effected by roundoff and those effected by failure to converge. However, there is no guarantee that it selects those in this regime, since in principle a mode could both be in the roundoff limit and have not converged yet. Yet when this is done, there are no discontinuities in F_{inf} for any of the l-modes when the median approach is used. See mode zero for an example. The maximum or the minimum may also be chosen.
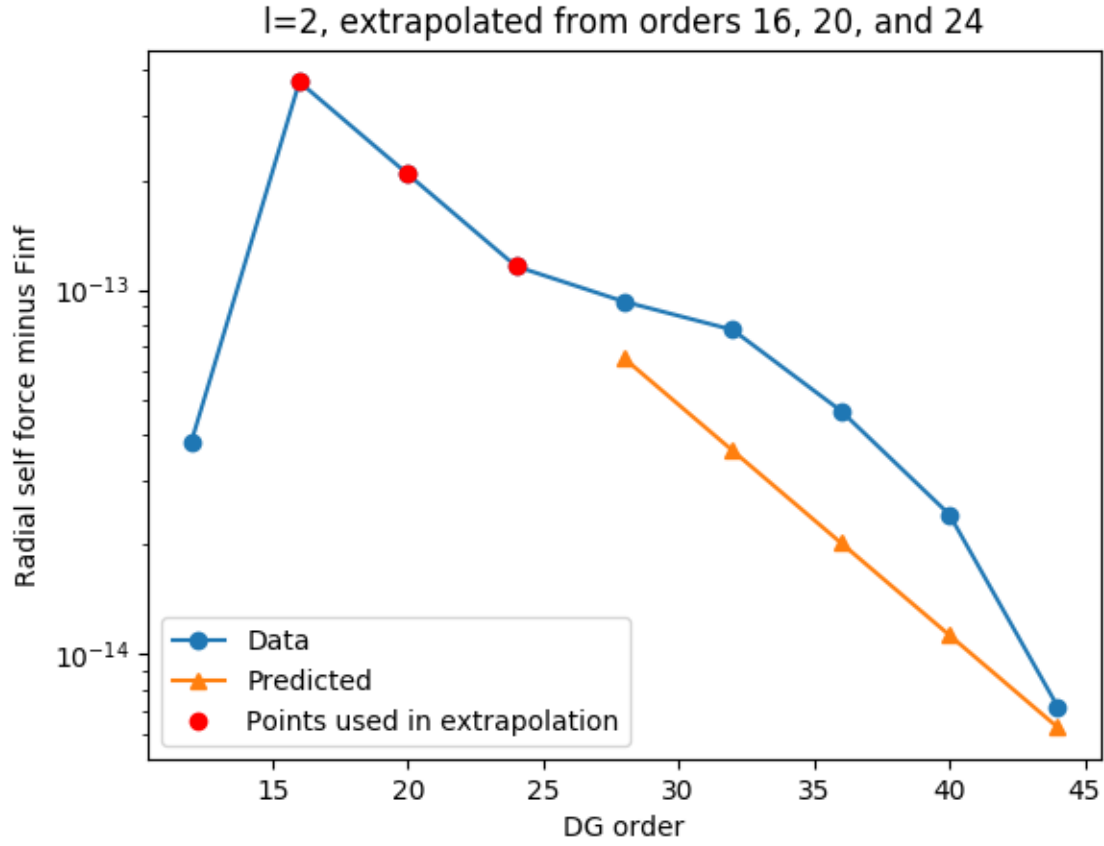
Figure 6.3: Fluctuation in one of the points chosen in the extrapolation, due to roundoff or truncation error, causes the extrapolation to predict a value of F_{inf} that is subtly wrong, leading to curvature in the semi-log plot after F_{inf} subtraction. t=632, l=2, i=1
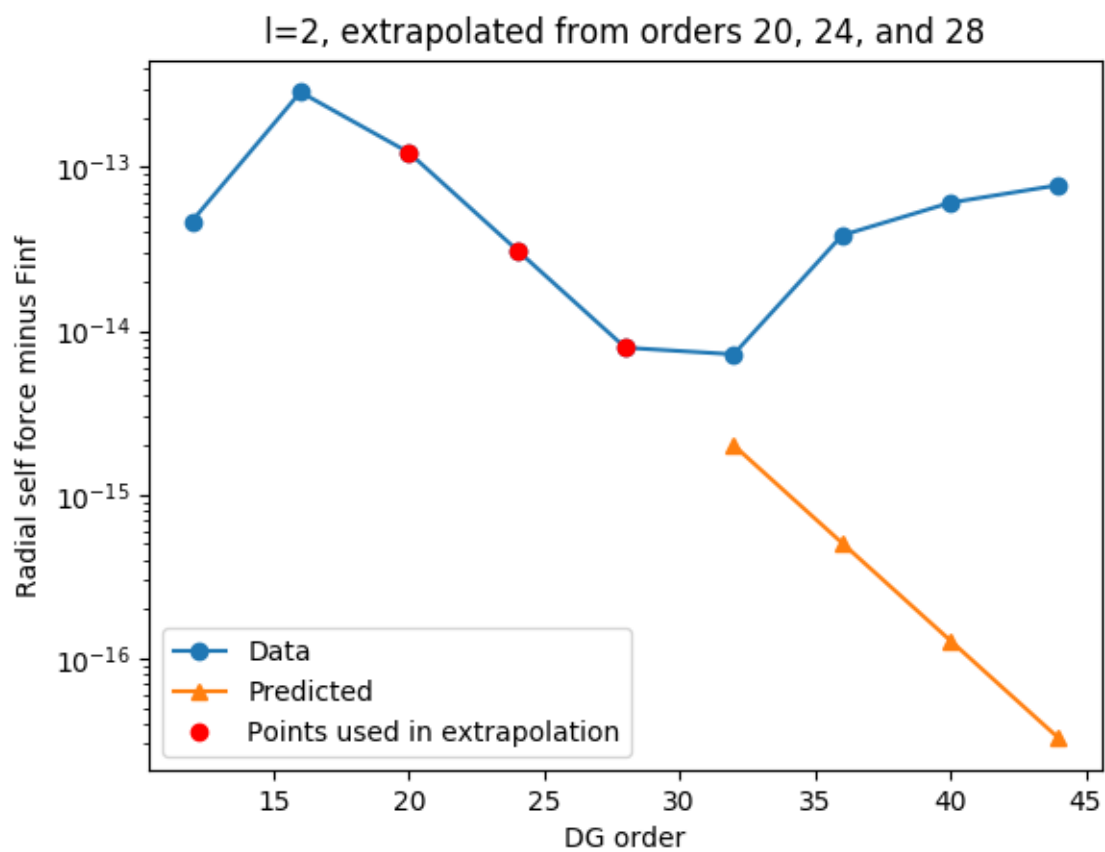
Figure 6.4: Roundoff error is visible at high DG orders. t=632, l=2, i=2
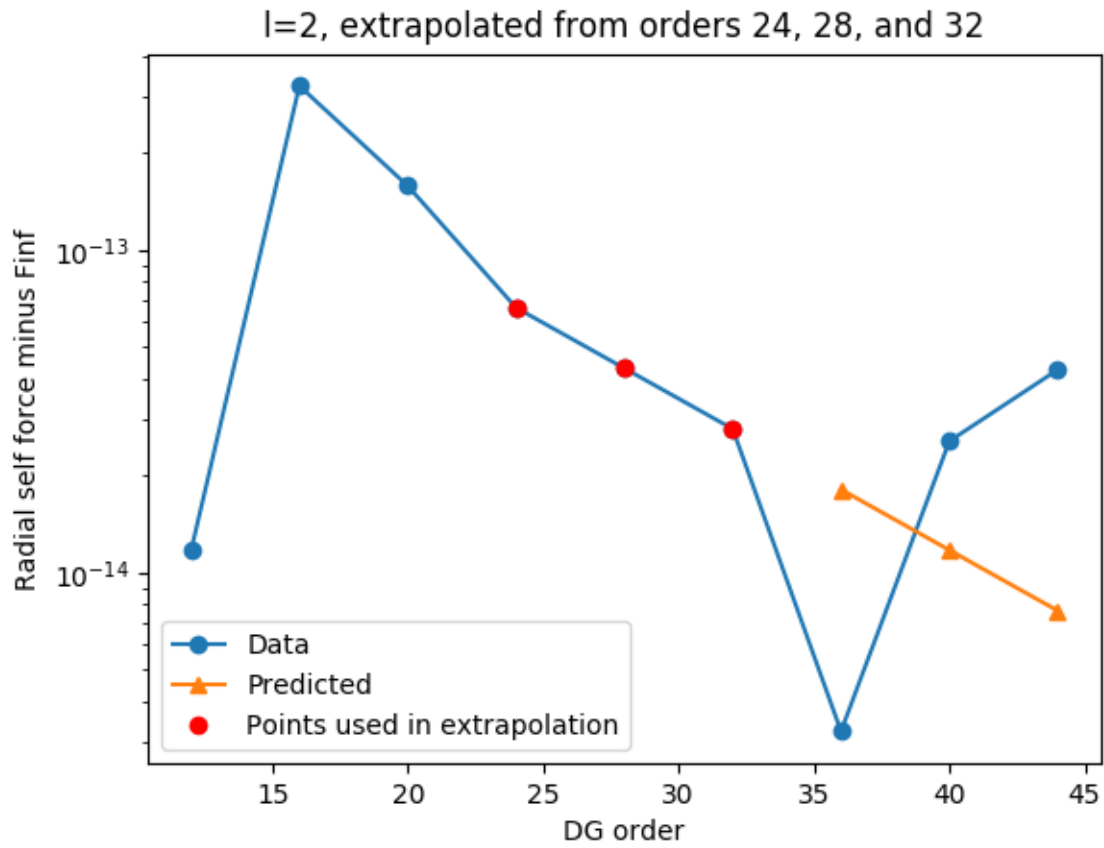
Figure 6.5: The incorrect value of F_{inf} has been chosen due to roundoff error, perhaps due to finite precision in the root finding algorithm, leading to a negative values, that show as a "V" in the semi-log plot. t=632, l=3, i=3
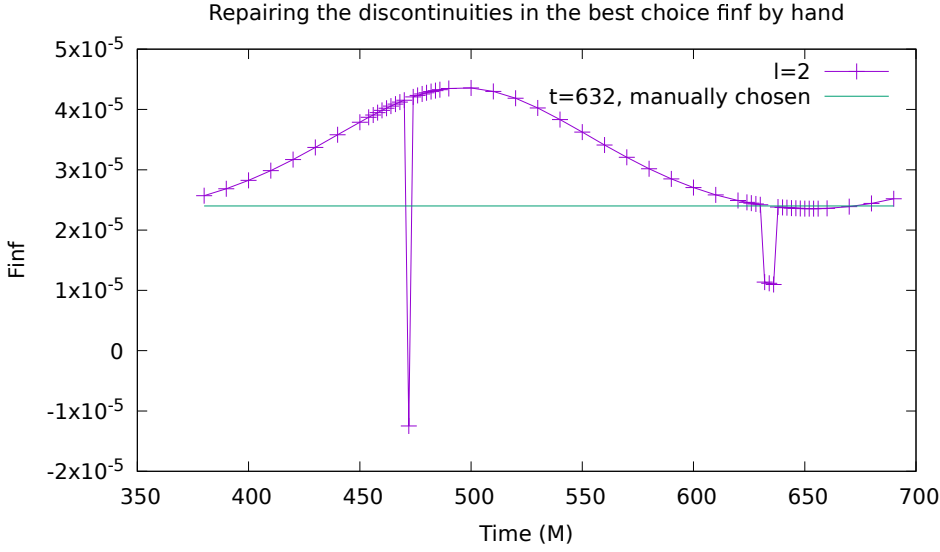
Figure 6.6: Manual correction for the discontinuities in the l=2 mode, using the manually determined F_{inf} data from Table 6.1.

6.0.2 Determining F_{inf} using maximum likelihood fits to subsegments of lines in semi-log space

A better motivated approach, is to fit subsegments of lines in semi-log space on the DG order convergence plot, and find the most linear, longest linear, region. A fit with the "best" value of the reduced chi squared should be a good approximation to this. The reduced chi squared is the value of the sum of the residuals of the fit squared divided by the number of degrees of freedom, which in this case is the number of points in the fit minus two, since there are two degrees of freedom in a linear fit. The expectation value of the reduced chi squared, in the limit of a large number of degrees of freedom, is one. I loop over starting and ending points of the fit, and over starting orders, and choose the starting order with the best fit line segment in the sense that that line segment has a reduced chi squared closest to one. An example of such an automatically chosen starting index is given in Figure ??, where there is a long exponentially converging region. Figure ?? shows that the absolute error between fit and median techniques increases with l-mode, possibly indicating that roundoff error becomes a more significant factor in the median technique as the l-mode increases, and the fit technique becomes more important.

44
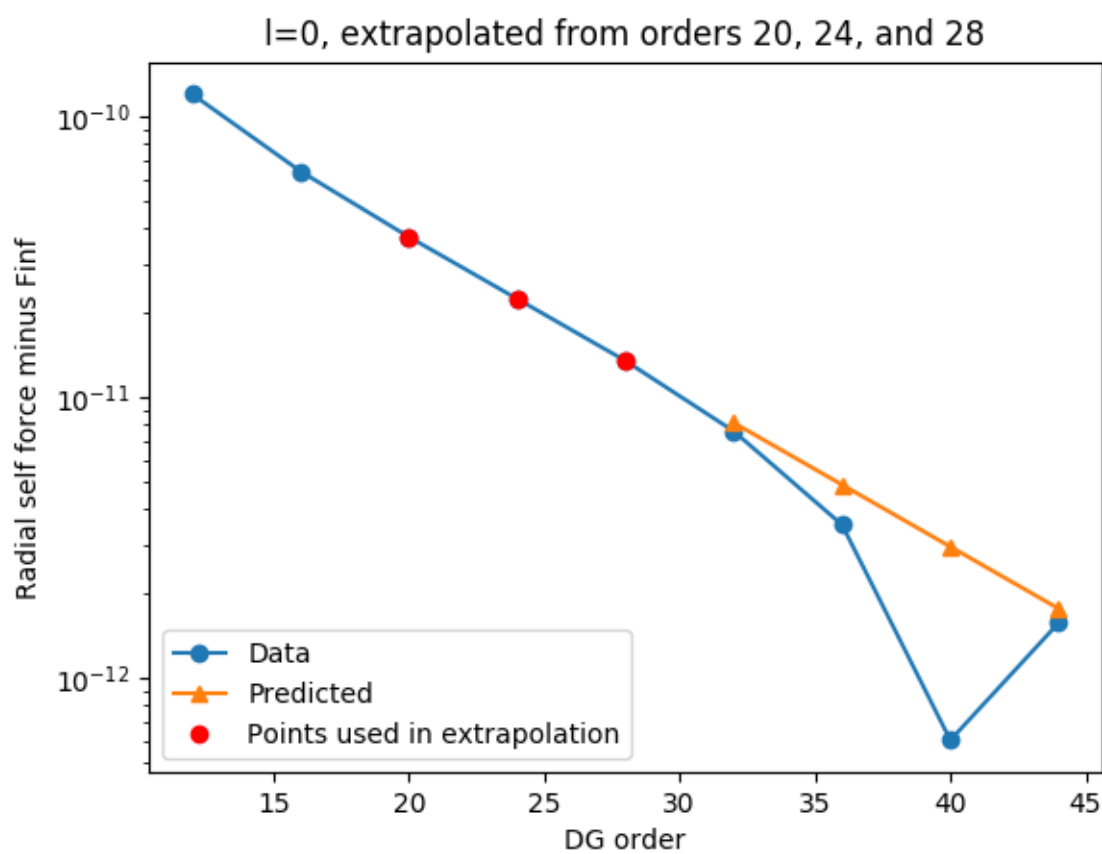
Figure 6.8: l=0 mode with line-segment fit-chosen starting order produces convergence plot with long exponentially converging region
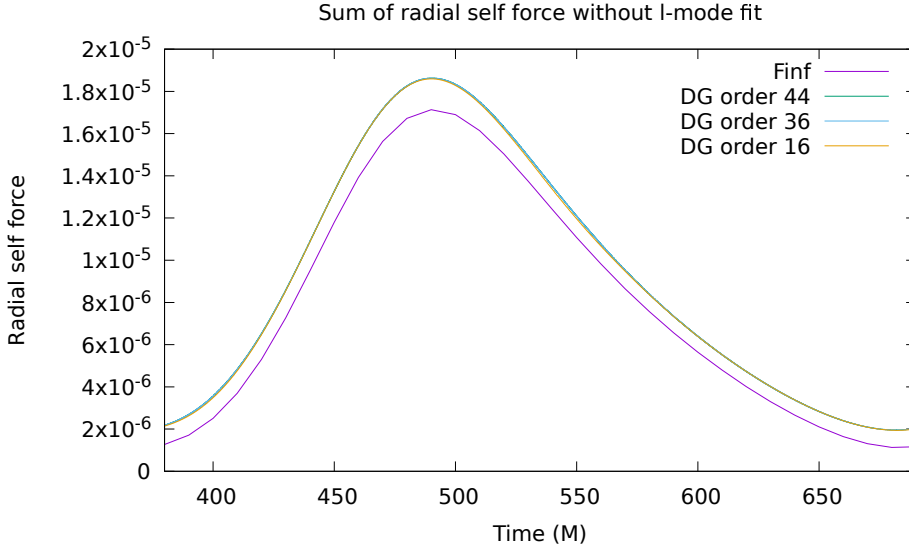
Figure 6.9: A comparison of F_∞ to several DG orders shows that they either do not converge rapidly toward F_∞ or there is a bug in the code.

6.0.3 Verification of the fit method fails

We expect that F_∞ should be the limit to which the DG orders are approaching, as order increases. Figure 6.9 shows F_∞ generated by the fit method and the median method, summed naively without an l-mode fit (see Chapter 7.4) as a function of time, in comparison to three DG orders. It is clear that there is a large gap between these DG orders and F_∞. I am unsure whether this is because the orders converge slowly to the limit, which seems unlikely since the few orders I have plotted are close together, or because there is a bug in the code. I favor the second hypothesis. The ultimate goal is to choose a suitable DG order with a small enough error relative to F_∞, at which to run all the code in the future.

I note that verification of the sum over all modes fails. Figure 6.11 demonstrates that the sum over modes for F_∞ does not match the closely converging other three DG orders shown. It would be difficult to fit an exponential through these three curves and reach F_∞ as an asymptote. Some offset is expected.

6.1 A third method

In a third approach, I consider the behavior of F_∞ as a function of starting order of the extrapolation. In many, but not all, modes, F_∞ appears to converge to an asymptote
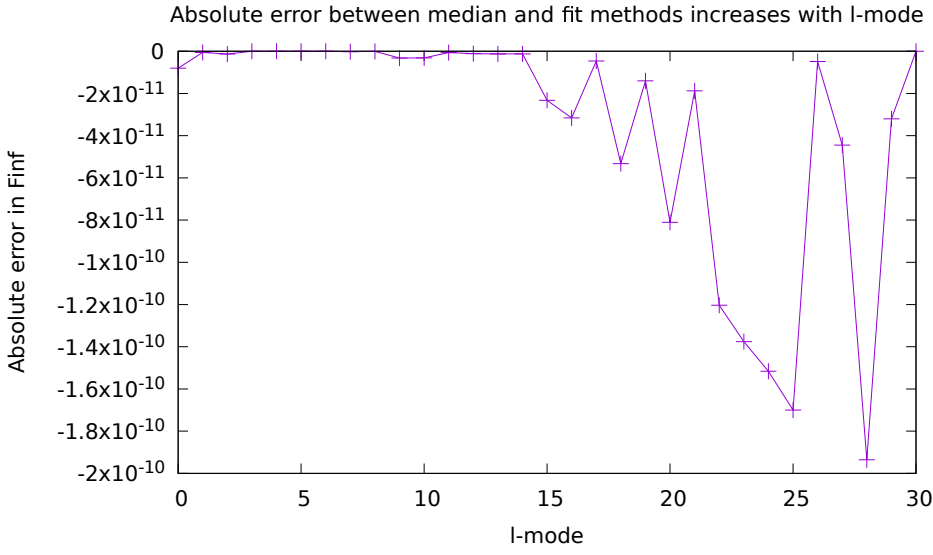
Figure 6.10: Absolute error between fit and median techniques increases with l-mode.
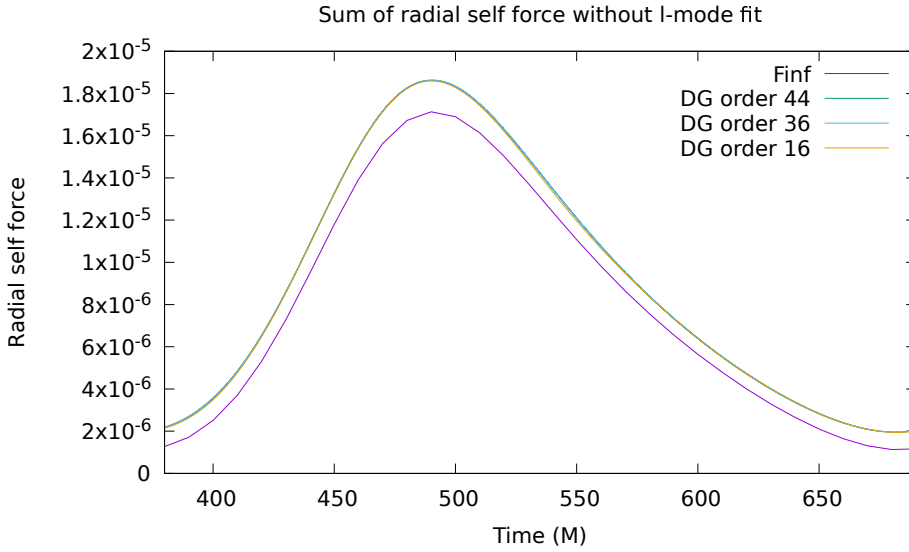
Figure 6.11: An exponential likely does not fit through these three curves with these orders and reach F_∞ as an asymptote, though some offset is expected.

from above or below as the DG starting order increases. However, in many modes, some starting orders produce no solution, so our set of six DG starting orders is reduced to somewhere between three and five. There are two obvious ways to test for convergence: fit an exponent or a power law and do a likelihood ratio test relative to a constant (since the second order errors are unmodelled), or, more reasonably, examine the signs of the first and second numerical derivatives and consider the end of the convergent regime to be the point where the roundoff noise dominates, and the derivative test no longer works. From this derivative sign test, we can determine the best starting order for F_∞ of a pattern of five or six points that are behaving in a converging like pattern.

However, sometimes, due to high roundoff noise or non-convergent behavior, a low DG order is chosen even for the case where there are five or six good contiguous starting indices. In that case, the asymptotic value of F_∞ at high DG orders is under-estimated. To achieve a better estimate, I sort this group into the same class as the two, three, and four length contiguous sets of successful DG orders that generated values of F_∞. For this case, I make an assumption that except for one or maybe two outliers, F_∞ is approximately constant across the range. The outliers may be at the beginning or the end, or may be due to roundoff noise fluctuations. To reject outliers, I do a standard statistical test of taking the average, making a veto based on the number of standard deviations a point is away from the average, and taking an average again using only the data that survived the veto. I select the point with the value closest to the second average as the best starting order for the extrapolation, and the value I will use to obtain F_∞. In this case, I found that I got linear curves of $\Psi_r - F_\infty$ on a semi-log scale for a one sigma veto.

After performing this selection of the best starting order, based on methods to look for asymptotes or reject outliers, I obtained the time evolution of the radial self force, summed from $l = 0$ to $l = 30$, shown in Figure 6.12. The absolute error between F_∞ and the different DG orders is shown in Figure 6.13 and the relative error is shown in Figure 6.14. There is one time where there is some kind of glitch in F_∞ that remains to be investigated;

49
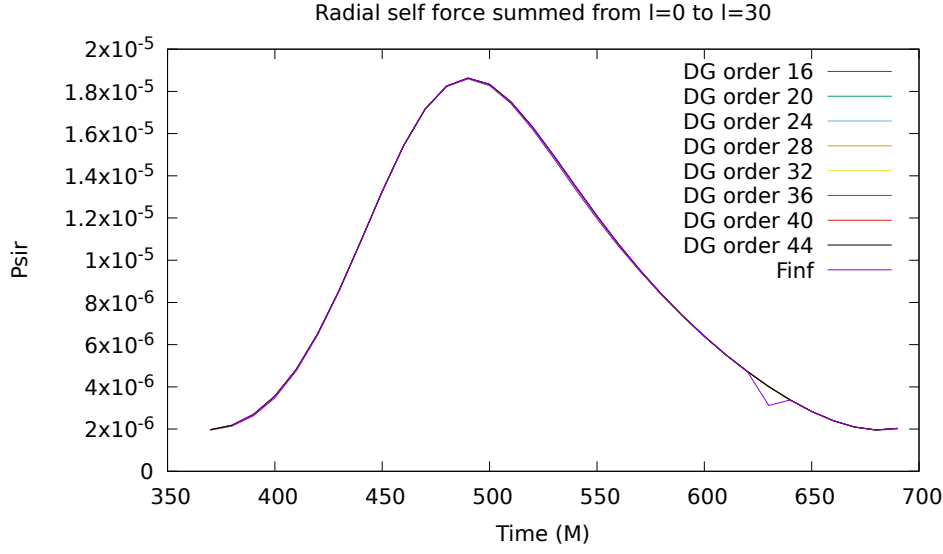
Figure 6.12: Sum from $l = 0$ to $l = 30$ of the radial self force, comparing all DG orders to F_∞. This was obtained using the method based on asymptotes and averages with rejection of outliers.

however, the evolution as a whole appears to be smooth. The absolute and relative error demonstrate that convergence is exponential until about DG order 36 or 40, and which point roundoff noise takes over. The best order for evolutions is therefore DG order 36.
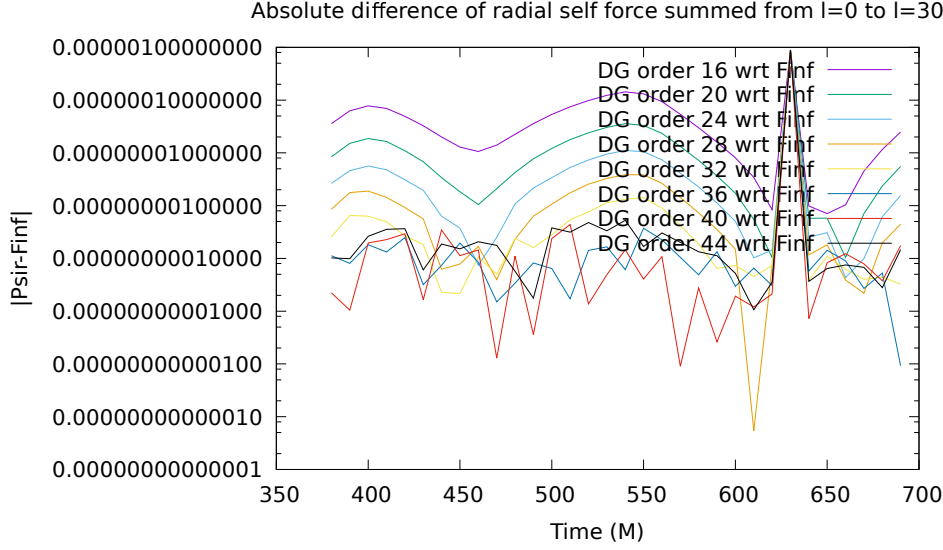
Figure 6.13: Absolute difference of the radial self force summed from $l = 0$ to $l = 30$ for each DG order compared to the total radial self force for these modes for F_∞. This was obtained using the method based on asymptotes and averages with rejection of outliers.
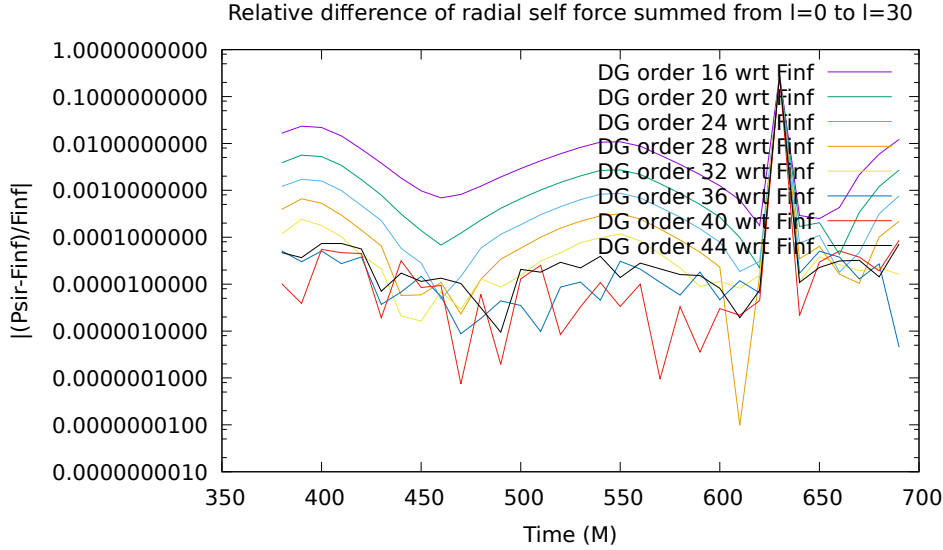
Figure 6.14: Relative difference of the radial self force summed from $l = 0$ to $l = 30$ for each DG order compared to the total radial self force for these modes for F_∞. This was obtained using the method based on asymptotes and averages with rejection of outliers.

Chapter 7
Extrapolating the mode-summed self-force to include contributions from an infinite number of spherical harmonic modes

In the last chapter, ψ_l was defined as the sum over m within a specific l-mode. To obtain the total self-force, it is necessary to sum all of these l-modes, for every time, using the value of F_∞ selected for that mode. Naively, one might sum only those modes for which there is data– only up to the maximum l-mode computed in the simulation. However, it is possible to do a fit to a functional form found in Reference [18] and use the analytic sum of that functional form to add the contribution from $l_{max}+1$ to infinity to the results computed from the simulation. The dependence of the m-summed self-force for a given mode on l is shown below, modified to omit terms that are rescaled to zero by the definition of the effective source in [**?**].

$$F_r(l) = \quad \frac{A}{(2l-1)(21+3)} + \frac{B}{(2l-3)(2l-1)(2l+3)(2l+5)}$$
$$+ \frac{C}{(2l-5)(2l-3)(2l-1)(2l+3)(2l+5)(2l+7)} + \cdots \tag{7.1}$$

Here A, B, and C are constants determined by a least squares fit. Least squares fits minimize the sum of the squared differences between the function and the data in the y direction, over all values of x_i. For fit parameters A, B, and C, and $l_max = n - 1$, the portion of the total radial self-force contributed by the l-modes extrapolated to infinity after the end of the known data is given by

$$\sum_n^\infty F_r(l) = \quad \frac{an}{4n^2-1} + \frac{bn}{3(9-40n^2+16n^4)}$$
$$\frac{cn}{5(2n-5)(2n-3)(2n-1)(2n+1)(2n+3)(2n+5)} + \cdots \tag{7.2}$$

Although Peter Diener's Fortran code implements this sum, I have analyzed it in an independent way to establish choices of l_{min} and l_{max} and to establish best choice DG orders for the code. In my computations, I have terminated the "end of the known data" at the end of the fit region, on the theory that I am simulating having more or fewer total l-modes available to me by including more or fewer l-modes in my fit.

Figure 7.1 shows a fit including the first three terms of this sum. Note how the fit is bad at high l. There are an infinite number of additional terms that can be added to the fit to account for this deviation. However, it is also fundamentally difficult to fit an exponentially converging function.

7.1 Fitting techniques and choice of starting mode

The quality of the fit depends on the number of terms in the l-mode sum used in the fit, as well as the starting and ending modes chosen. It is also very difficult to fit a nearly power law decay with relative error that does not decrease much at small values, which we might expect as long as the l-modes are in the truncation error regime. This is because a least squares fit minimizes distances between the curve and the data in a linear scale plot, not a log-log plot, giving disproportionate weight to data near the maximum of a power law decay. To correct this, I have suggested an alteration to the fit. I minimize the classic χ^2 with weights, as follows

$$\chi^2 = \sum_i \frac{(y_i - f(x_i))^2}{\sigma_i^2} \tag{7.3}$$

Since the σ_i weights do not represent proper statistical uncertainties, the normalization of the weights is unimportant, unless they are used to interpret the "goodness" of a fit in terms of a reduced chi-squared. Since the error behaves in an unknown, possibly highly correlated, deterministic, manner, cation is warranted in doing so. I have examined weights that are constant (effectively no weight), that scale as l^{-2}, and that scale as l^{-1}. The first is motivated by standard fitting techniques and is the default solution, while the second is motivated by the nature of the first order scaling behavior of the function to which we fit
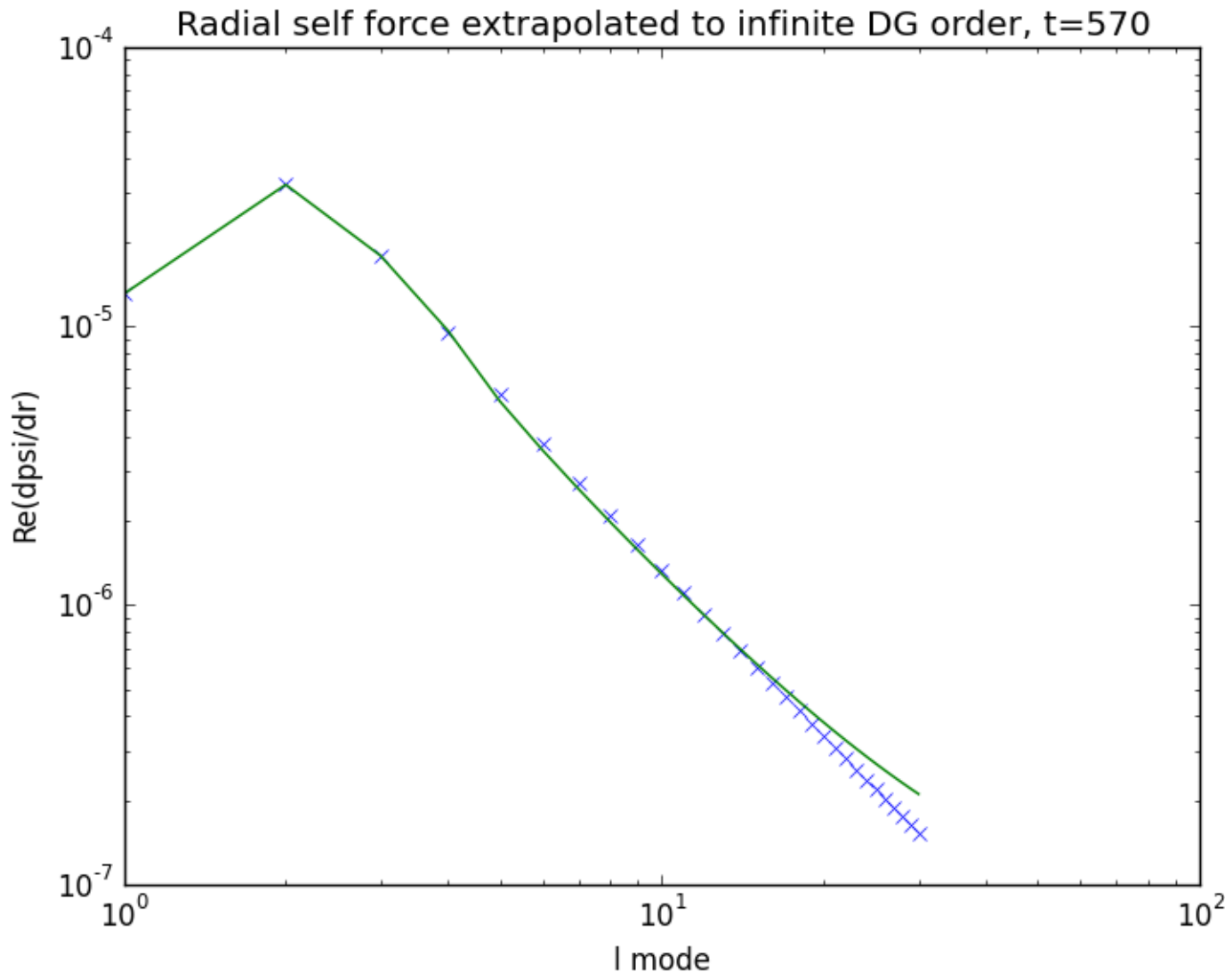
Figure 7.1: Three term fit of l-mode vs F_{inf}.

the l-modes, and the third is motivated by the desire to find something that behaves well in both the truncation error and roundoff error regimes. Figure 7.2 shows the functional form of the l-mode fit with three different choices of weights. Figures 7.3 and 7.4 show that for all choices of weight scaling, a starting l-mode of 14 is a reasonably good fit, while significantly lower starting modes are a bad fit for three terms in the l-mode fit expansion. These figures also show that the choice of sigma can make a small difference in the goodness of the fit at high l-mode, which is important for extrapolation to infinite l-mode. However, Figure ?? shows that for a range of l_{min} versus l_{max}, the variation in the total radial self force due to variation over start and stop range in the fit is small compared to the variation between between l^{-2} scaling and constant scaling (circles and triangles).

7.2   Roundoff noise and choice of end mode

In Figure 7.6 roundoff noise is evident at higher l_{max} choices, where l_{min} is the minimum l-mode included in the fit and l_{max} is the maximum l-mode included in the fit. This is true of most times near aphelion. Note that there is not a large difference between two and three terms, and that four terms is less smooth a surface, suggesting that it is more subject to round off noise. Three terms is preferred. In Figure 7.7, a smaller region of l_min versus l_max space has been chosen to form the surface plot, and the roundoff noise is excluded.

7.3   Results and errors

Figure 7.8 shows the evolution of the total self force over time. First it has been extrapolated to obtain F_∞ using the three-point DG order exponential convergence extrapolation technique, and the optimal starting order has been chosen. Then the modes computed in the simulation have been summed numerically from $l = 0$ up to some l_{max}, and a fit from l_{min} to l_{max} has been used to extrapolate the sum to infinite l, to obtain the total radial self-force, at each time. The three different measurement techniques described
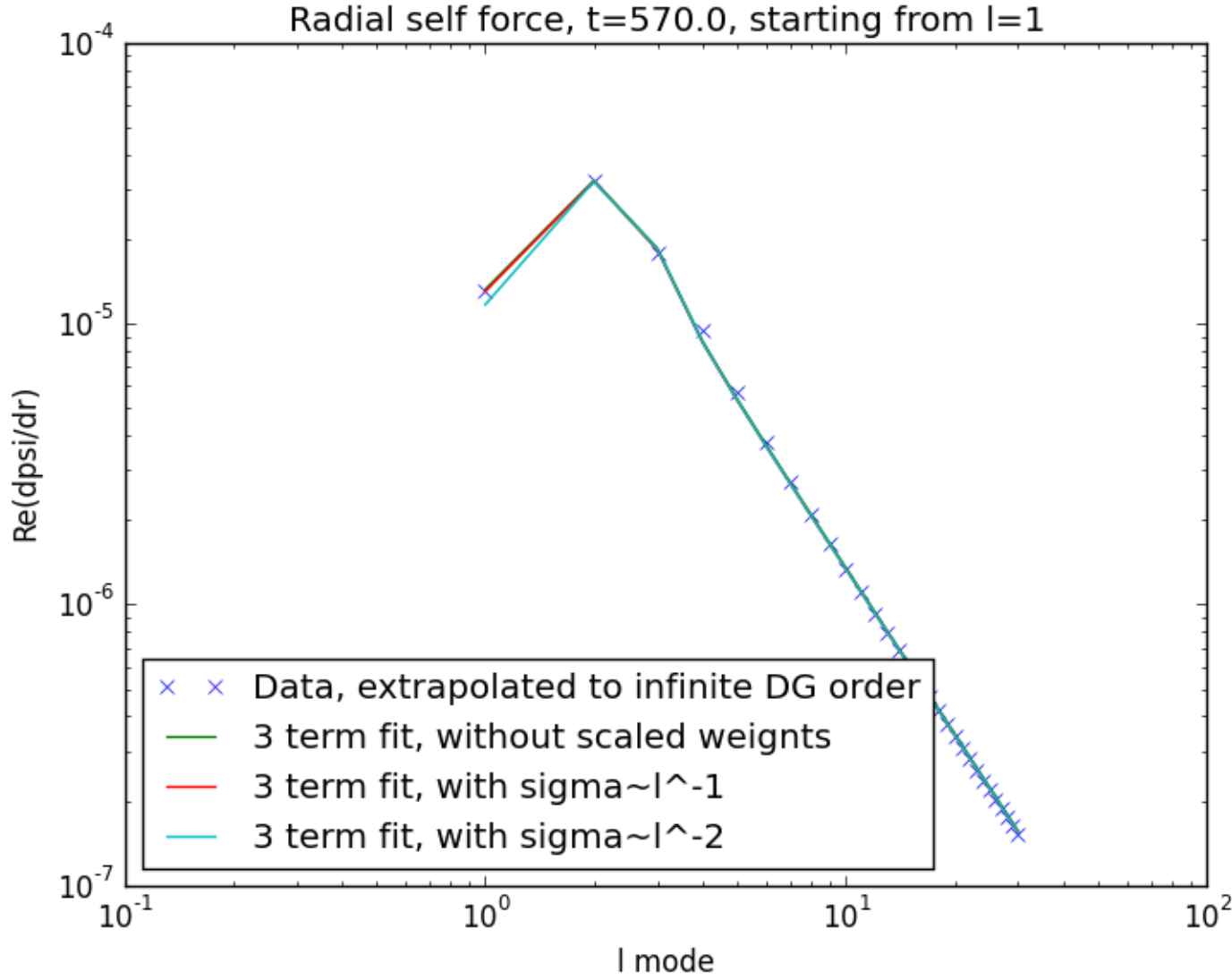
Figure 7.2: The l-mode convergence behavior and three different fits to it using three terms in the l-mode fit sum of Equation 7.1. The three different fits represent different choices of weights in the least squares fit. It appears that starting the fit at 14 might level this residual.
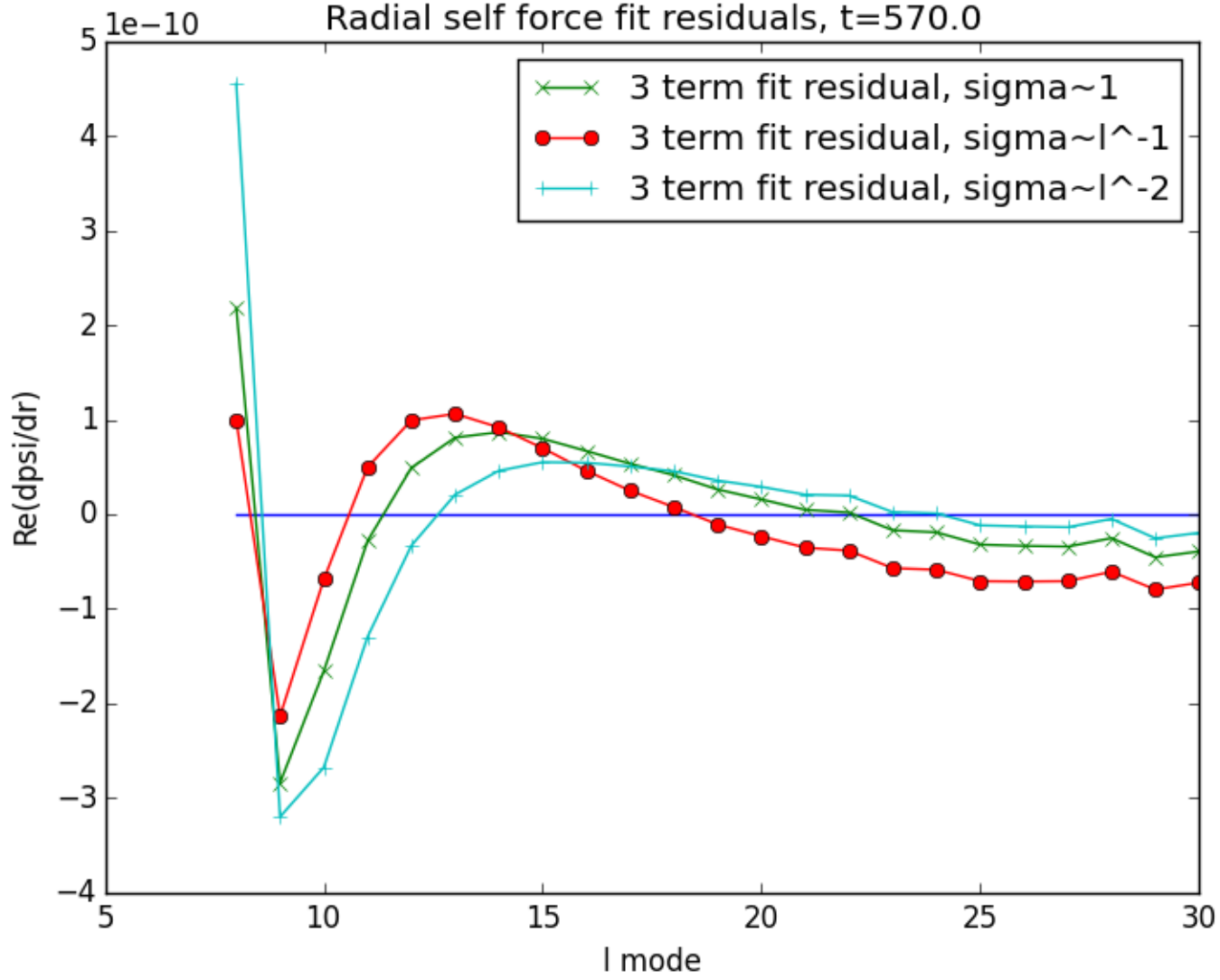
Figure 7.3: Fit residuals for three different least squares weight scalings starting from $l_{min} = 8$. Notice that this is a bad fit, due to the strong correlated skews to either side of the axis.
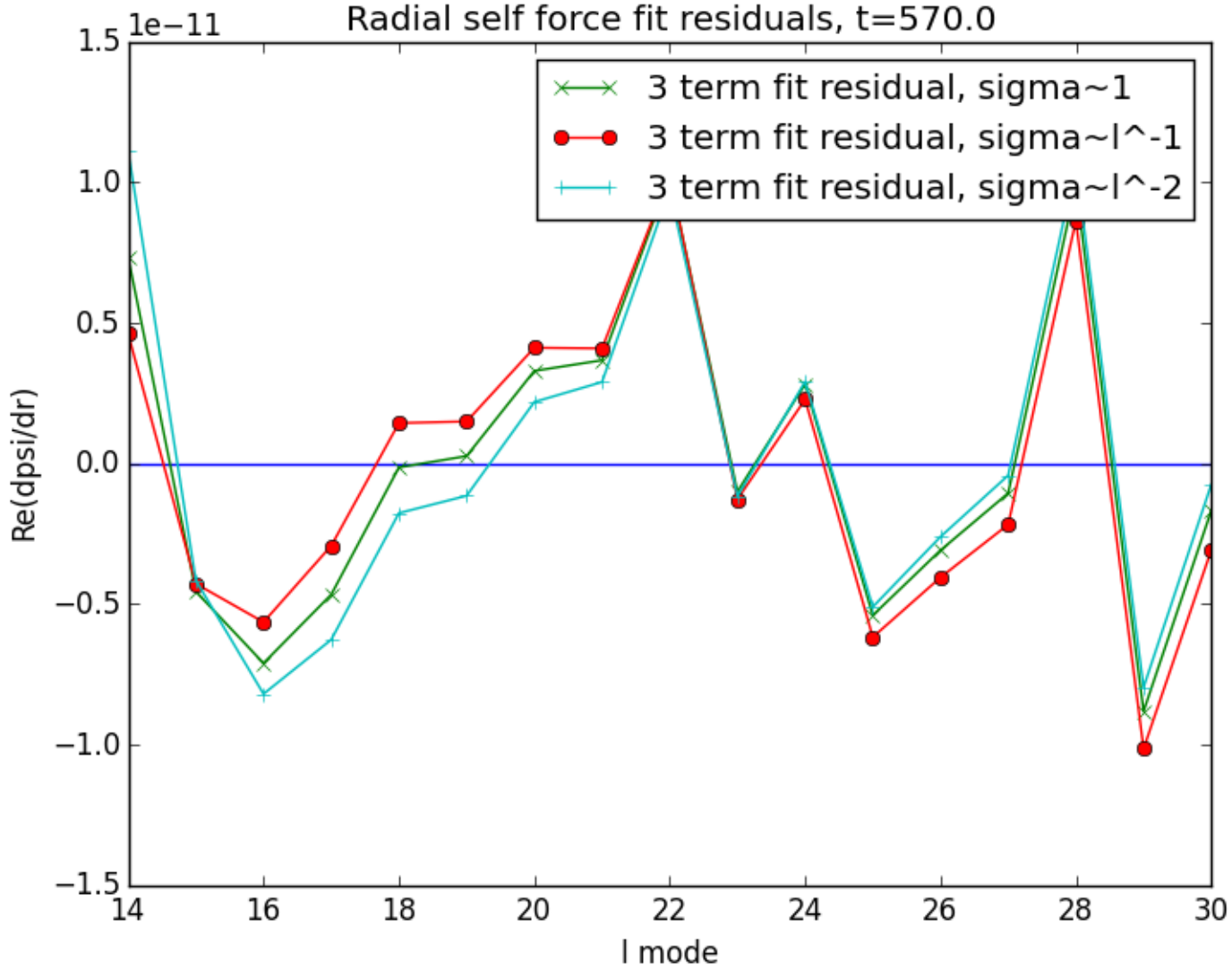
Figure 7.4: Fit residuals for three different least squares weight scalings starting from $l_{min} = 14$. This is a much better fit than $l_{min} = 8$ both due to the smaller correlated deviations from zero and due to the smaller amplitude of the residual.
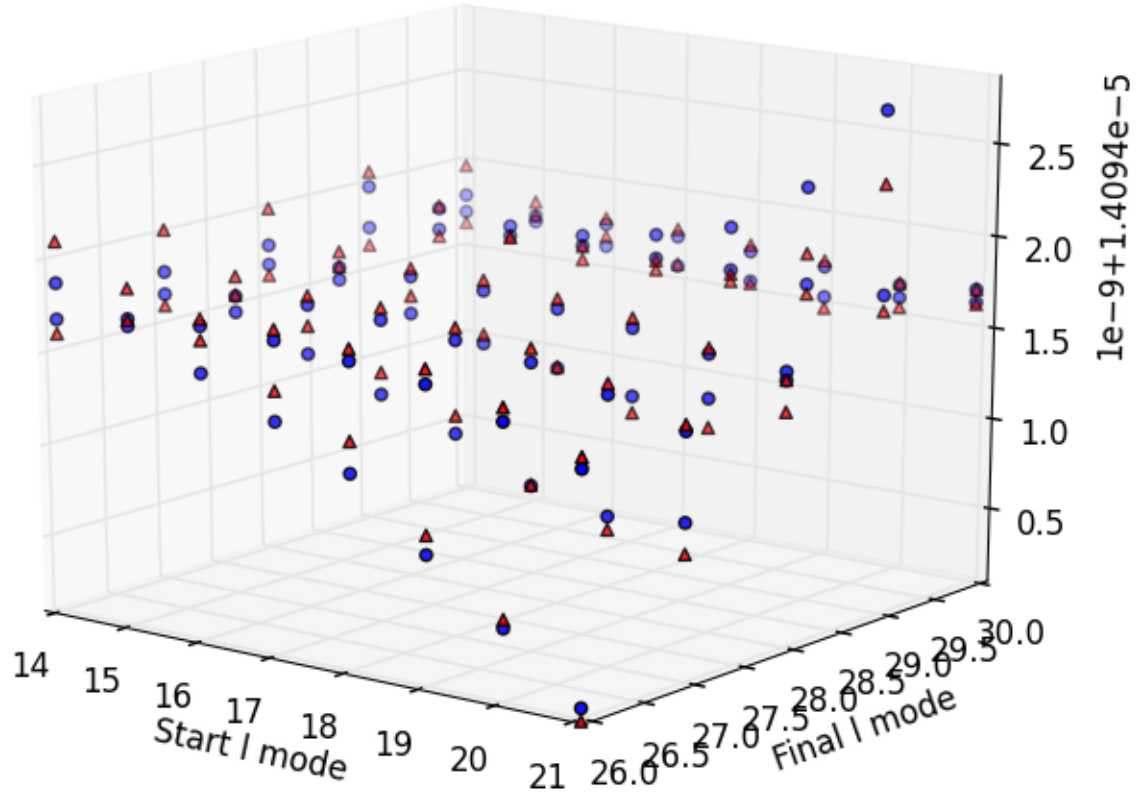
Figure 7.5: The difference between the triangles and the circles shows that the difference in the total radial self force between the presence of a $\sigma \sim l^{-2}$ weight and no weight is unimportant compared to the difference in the total radial self force between various start and end points of the l-mode fit.
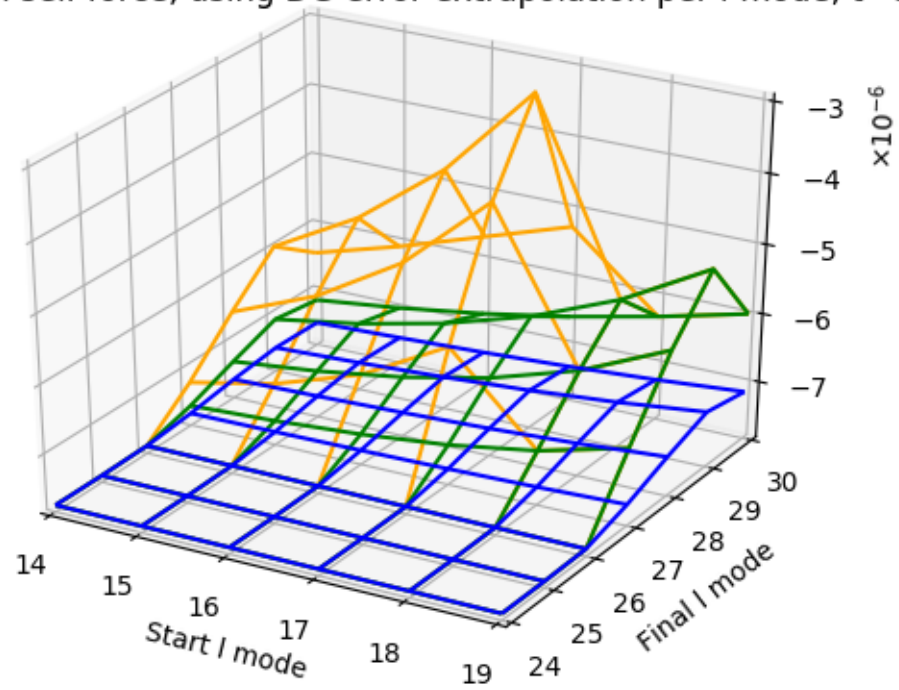
Figure 7.6: t=635, 2, 3, and 4 term fits over a broad range of lmin and lmax values. Note the roundoff noise at high lmax. Aphelion, where this effect is worst.
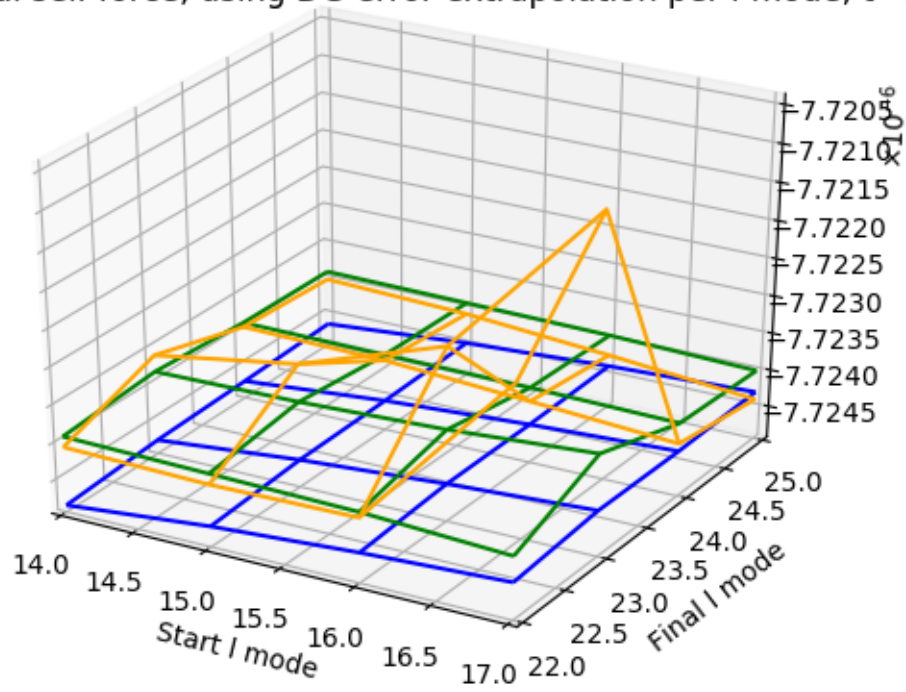
Figure 7.7: t=635, 2, 3, and 4 term fits over a small range of l_{min} and l_{max}. Aphelion. No roundoff noise in this range.
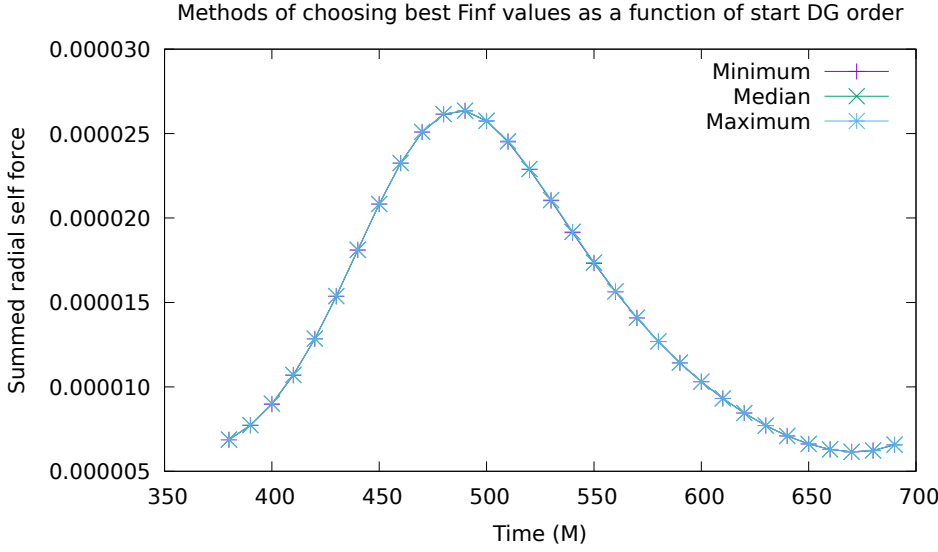
Figure 7.8: This is the actual summed, doubly extrapolated, radial self force, measured using the minimum, maximum, and median method for selecting the best starting order.

7.3.1 Relative and absolute differences

Figure 7.9 shows the relative difference between the total radial self force measured in two different ways. The self-force values in each surface plot shown in Figures 7.6 and 7.7 were averaged to obtain better estimates of the total radial self force as a function of time. This plot shows the relative difference. Some caution is advised in interpretation, since the relative difference may largely point to roundoff noise in the larger range. It is clearly random, and clearly decreasing with time, but also very clearly not at the machine precision level necessary to be roundoff noise.

Figure 7.10 shows the relative difference between using two and three terms in the fit to compute the total radial self force, as a function of time. Again, this is random, decreasing with time, and not at the machine precision level.

In Figure 7.11, the purple line is the relative difference between the maximum and the median, and the green line is the relative difference between the median and the minimum. The first is subject to roundoff error due to the potential for the DG order with the maximum self-force, which is likely the maximum DG order, to contain roundoff error. The second is subject to effects due to failure to hit the regime where the truncation error
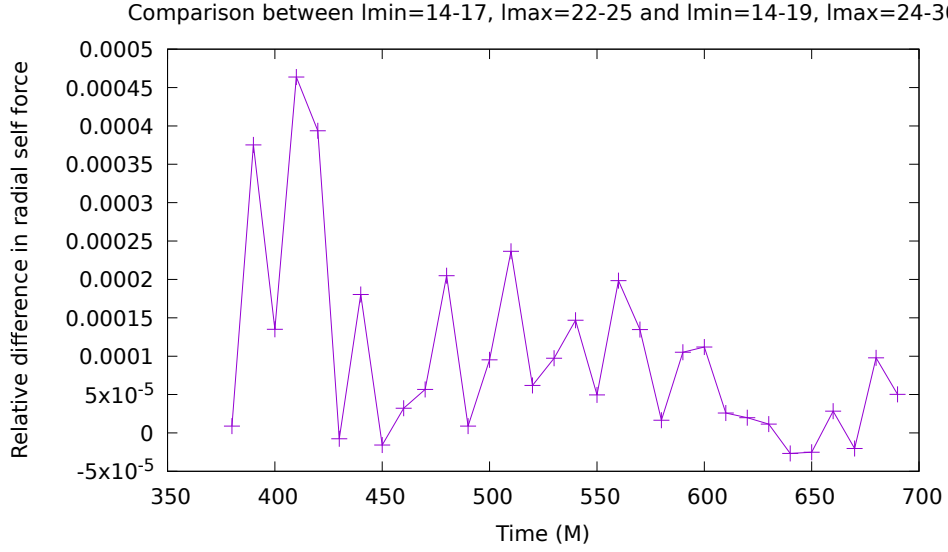
Figure 7.9: The relative difference between total self force determined by averaging large versus small ranges of total radial self-force l_{min}, l_{max} surfaces, as a function of time.
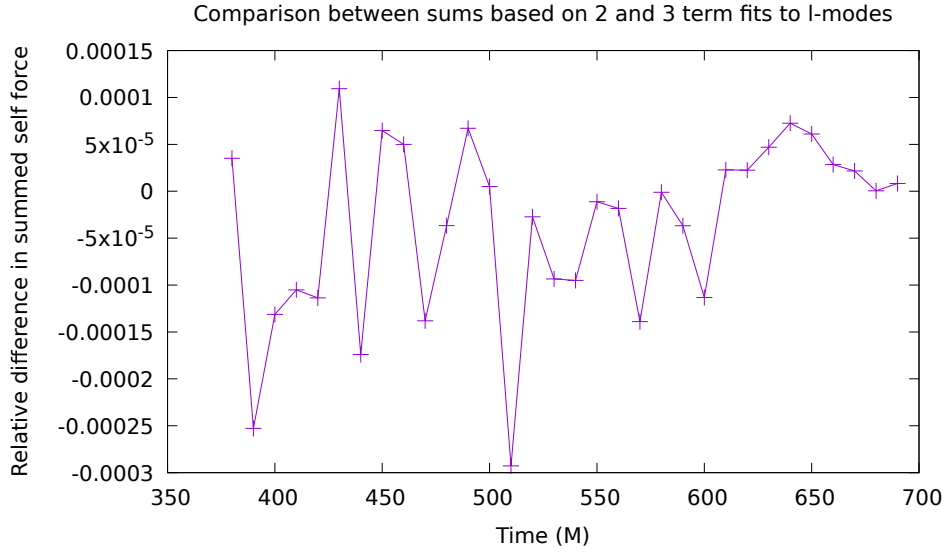
Figure 7.10: The relative error of the total radial self-force, comparing two to three terms in the l-mode fit.
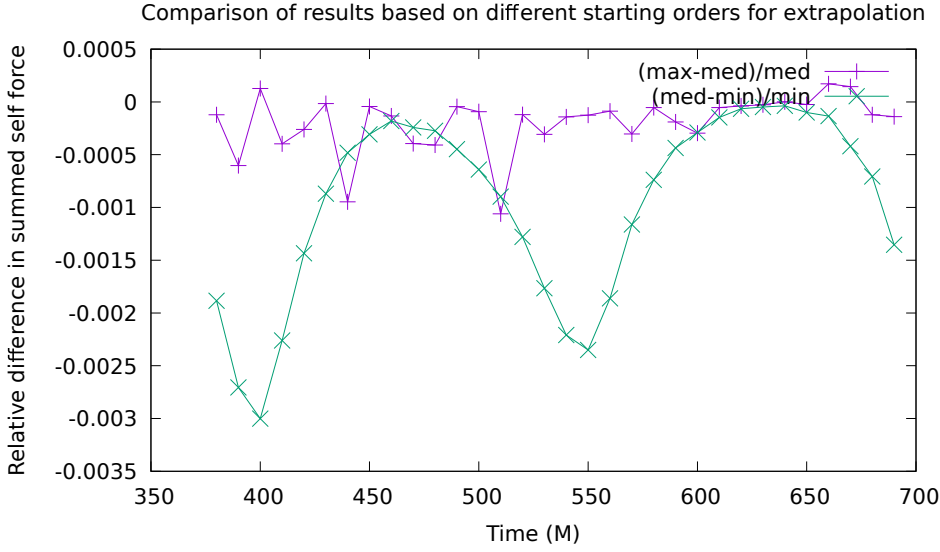
Figure 7.11: The relative error between median, the maximum, minimum methods of determining the starting order, summed over l-mode to obtain the total self-force and evolved over time.

model is valid, because of the minimum.

7.3.2 Fractional errors

I obtain the fractional error, within a given method for choosing the best self force, by dividing the standard deviation of the total self-force, over a range of l_{min} and l_{max} by the average. This is shown for median and fit methods in Figures 7.12 and 7.13, respectively. The absolute error is the standard deviation itself. The absolute error, as a function of time, compared to the self-force itself, is shown in Figure 7.14. The two peaks do not obviously match perihelion, aphelion, or any specific phase of the orbit.

7.4 Best choice l_{mins} and l_{max}'s and best choice DG orders

My conclusion is that l_min can be as low as 14 and as high as 17, and l_max can be as low as 22 and as high as 25 without encountering roundoff or truncation error. There is no single best choice of DG order for a given mode or time, that I have yet been able to establish. It would be quite difficult, in terms of infrastructure, to run multiple DG orders
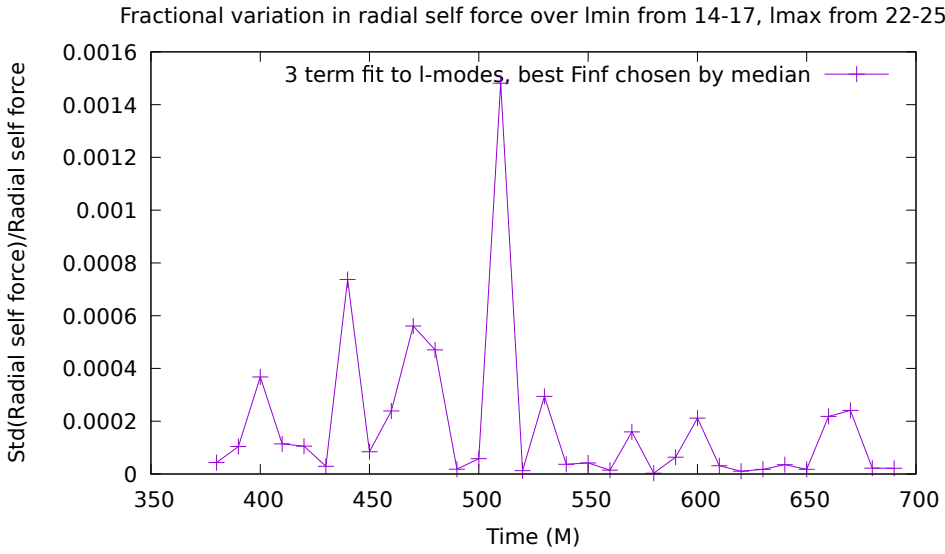
Figure 7.12: Fractional error, 3 term, median method.
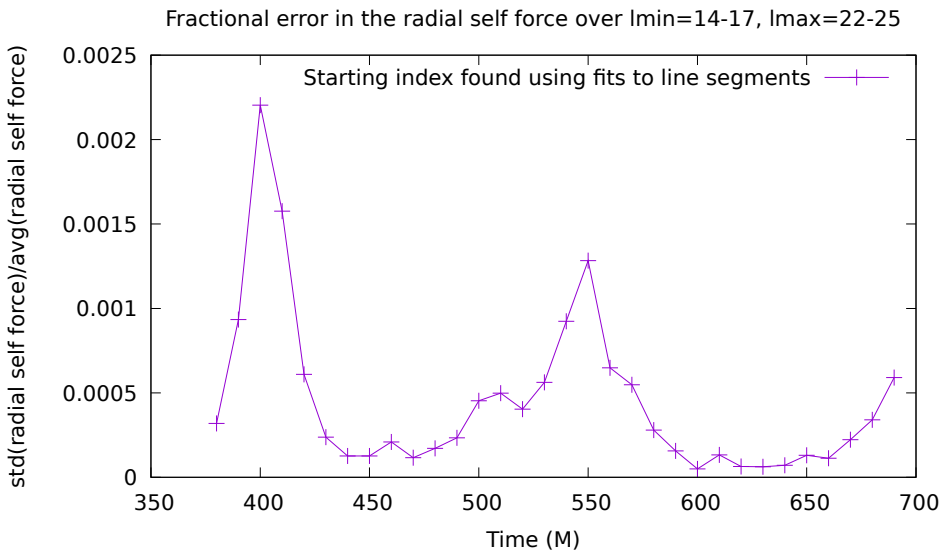
Figure 7.13: Fractional error, 3 term, fit method

65
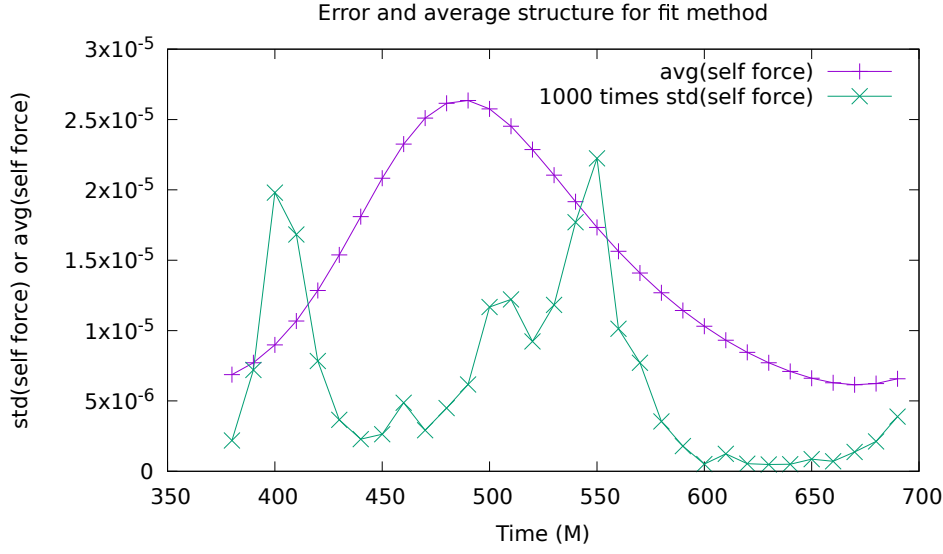
Figure 7.14: The structure of the absolute error in comparison to the evolution in time for the fit method.

at the same time.

To obtain the best possible DG order for all times and for all l-modes is not theoretically possible. F_{∞} is a function of l-mode and time. However, it may be possible to choose a DG order for which a constant offset in time and mode is best, even if that offset is itself not meaningful, unlike F_{∞}. This can be done manually and graphically, and that is the next step.

Chapter 8
Future work: generic orbits via the osculating orbits framework

8.1 Plans for the more distant future

First, I will update our comparison study with Niels Warburton's geodesic code, to higher l-modes and more recent versions of both codes and report the results to Niels Warburton and Peter Diener.

I also plan to run Peter Diener's simulation of scalar self-force on a Schwarzschild background for generic orbits and examine the data, with the purpose of understanding the physical implications of the output of the simulation. If necessary, I may help debug the simulation. Peter Diener, Ian Vega, Barry Wardell, and Steven Detweiler [?] have previously published on self-consistent evolution of a particle around a Schwarzschild black-hole; however, the current goal is to reimplement the same thing more precisely, in 1 dimension with spherical harmonics instead of in 1+3 dimensions and using the Discontinuous Galerkin method.

8.2 Generic orbits

To extend the wave equation to that produced by a particle on a self-consistent orbit, it is necessary to include several additional effects.

$$(\Box - \xi R)\Psi^{ret} = -4\pi q \int \delta_4(x, z(\tau'))d\tau' \tag{8.1}$$

$$ma^\alpha = q(g_{(0)}^{\alpha\beta} + u^\alpha u^\beta)\Psi_{,\beta}^R \tag{8.2}$$

$$\frac{dm}{d\tau} = -qu^\alpha\Psi_{,\alpha}^R \tag{8.3}$$

R is the Ricci scalar (0 in Schwarzschild space-time) and ξ is the coupling to curvature. The first equation gives th scalar wave equation in curved space-time, with a source. The

67

second equation gives the back-reaction due to acceleration of the particle. Here, Ψ^R is the regularized field. The third equation governs the self-consistent evolution of the mass of the particle. [56]

There are two methods for evolving the orbit that we may use, already implemented in the code by Peter Diener: geodesic evolution and osculating orbits **??**.

8.2.1 Geodesic evolution

The geodesic equation is modified to include a force term on the right hand side in the presence of a self-force or external force [**?**].

$$\frac{d^2x^\mu}{d\tau^2} + \Gamma^\mu_{\rho\sigma}\frac{dx^\rho}{d\tau}\frac{dx^\sigma}{d\tau} = qF^\mu_\nu\frac{dx^\nu}{d\tau} = a^\mu \tag{8.4}$$

This equation, together with Equations 8.3, provide the basis for the generic evolution code when the geodesic evolution method is used.

8.2.2 Osculating orbits

An alternative approach is possible, based upon Reference [44]. In an evolving orbit, the angular momentum and energy of a particle are only approximate symmetries, but extracted far away, they become measurable quantities. It is natural to evolve in a physical process that is closely related to these quantities. The eccentric orbit geodesic parameters p and e (semilatus rectum and eccentricity) are chosen (see Chapter 5.4 In the self-consistent evolution, the orbit is accelerated from one geodesic to a neighboring geodesic, and gradually evolves through touching geodesics over time. In this process, p and e are updated via a series of ordinary differential equations with extraordinarily complicated right hand sides. This is done using the same RK4 routine that is used to solve the wave equation.

References

[1] Amaro-Seoane, Pau; Gair, Jonathon R.; Pound, Adam; Hughes, Scott A.; Sopuerta, Carlos F. (2014). Research Update on Extreme-Mass-Ratio Inspirals. *arXiv:1410.0958v1*.

[2] Babak, Stanislav. (2017). Science with the space-based interferometer LISA. V: Extreme mass-ratio inspirals. *arXiv:1703.09722v1*.

[3] Bambi, Cosimo. (2017) Testing black hole candidates with electromagnetic radiation. *Reviews of Modern Physics* 89.

[4] Bernuzzi, Sebastiano; Nagar, Alessandro; Zenginoglu, Anil. (2011). Binary black hole coalescence in the large-mass-ratio limit: the hyperboloidal layer method and waveforms at null infinity. *arXiv:1107.5402v2*.

[5] Berti, Emanuele; Cardoso, Vitor; Starinets, Andrei O. Quasinormal modes of black holes and black branes. *arXiv:0905.2975v2*

[6] Carroll, Sean M. (2004). *An Introduction ot General Relativity Spacetime and Geometry.* Addison Wesley.

[7] Danzmann, Karsten. (2017). LISA Laser Interferometer Space Antenna: A proposal in response to the ESA call for L3 mission concepts.

[8] Damour, Thibault. (2015). 1974: the discovery of the first binary pulsar. *arXiv:1411.3930v2*.

[9] Diener, Peter; Vega, Ian; Wardell, Barry; Detweiler, Steven. Self-consistent orbital evolution of a particle around a Schwarzschild black hole. *arXiv:1112.4821v3*.

[10] Dirac, P. A. M. (1938). Classical theory of radiating electrons. *Royal Society Publishing.*

[11] Diaz-Rivera, Luz Maria; Messaritaki, Eirini; Whiting, Bernard F.; Detweiler, Steven. (2004). Scalar field self-force effects on orbits about a Schwarzschild black hole. *arXiv:gr-qc/0410011v1*.

[12] Field, Scott E.; Hesthaven, Jan S.; Lau, Stephen R. Discontinuous Galerkin method for computing gravitational waveforms from extreme mass ratio binaries. *arXiv:0902.1287v2*.

[13] Gillessen, S. ; Eisenhauer, F.; Fritz, T. K.; Bartko, H.; Dodds-Eden, K.; Pfuhl, O.; Genzel, R. (2009). The orbit of the star S2 around SGR A^* from VLT and Keck data. *arXiv:0910.3069v1*.

[14] Gair, Jonathan R.; Porter, Edward K. (2012). Observing extreme-mass-ratio inspirals with eLISA/NGO. *arXiv:1210.8066v1*

[15] Gralla, Samuel E.; Harte, Abraham I.; Wald, Robert M. (2009). A Rigorous Derivation of Electromagnetic Self-force. *arXiv:0905.2391v2.*

[16] Guzzetti, M.C.; Bartolo, N.; Liguori, M.; Martarrese, S. (2016). Gravitational waves from inflation. *arXiv:1605.01615v3.*

[17] Heffernan, Anna. (2012). The Self-Force Problem: Local Behavior of the Detweiler-Witing Singular Field. University College Dublin. *arXiv:1403.6177v1.*

[18] Heffernan, Anna; Ottewil, Adrian; Wardell, Barry; (2013). High-order expansions of the Detweiler-Whiting singular field in Schwarzschild spacetime. *arXiv:1204.0794v4.*

[19] Hesthaven, Jan S.; Warburton, Tim. (2008). *Nodal Disconintuous Galerkin Methods: Algroithms, Analysis, and Applications.* Springer.

[20] Hobbs, George; Dai, Shi. (2017). A review of pulsar timing array gravitational wave research. *arXiv:1707.01615v1*

[21] LIGO Virgo Collaboration. (2016). Observation of Gravitational Waves from a Binary Black Hole Merger. *Phys. Rev. Lett.* 116, 061102.

[22] LIGO Virgo Collaboration. (2016). GW151226: Observation of Gravitational Waves from a 22-Solar-Mass Binary Black Hole Coalescence. *Phys. Rev. Lett* 116, 241103.

[23] LIGO Virgo Collaboration. (2017). GW120104: Observation of a 50-Solar-Mass Binary Black Hole Coalescence at Redshift 0.2. *Phys. Rev. Lett.* 118, 221101.

[24] LIGO Virgo Collaboration. (2016). Observing Gravitational-wave Transient GW150914 with Minimal Assumptions. *Phys. Rev. D* 93, 122004.

[25] LIGO Virgo Collaboration. (2016). GW150914: First Results from the Search for Binary Black Hole Coalescence with Advanced LIGO. *Phys. Rev. D* 93, 122003.

[26] LIGO Virgo Collaboration. (2016). The Rate of Binary Black Hole Mergers Inferred from Advanced LIGO Observations Surrounding GW150914. *Accepted Astrophys. J. Lett*

[27] LIGO Virgo Collaboration. (2016). Astrophysical Implications of the Binary Black-Hole Merger GW150914. *Astrophys. J. Lett* 818, L22.

[28] LIGO Virgo Collaboration. (2016). Tests of General Relativity with GW150914. *Phys. Rev. Lett.* 116, 221101.

[29] LIGO Virgo Collaboration. (2016). GW150914: Implications for the Stochastic Gravitational Wave Background from Binary Black Holes. *Phys. Rev. Lett.* 116, 131102.

[30] LIGO Virgo Collaboration. (2016). Calibration of the Advanced LIGO Detectors for the Discovery of the Binary Black-hole Merger GW150914. *Submitted to Phys. Rev. D.*

[31] LIGO Virgo Collaboration. (2016). Characterization of Transient Noise in Advanced LIGO Relevant to Gravitational Wave Signal GW150914. *Class. Quant. Grav.* 33, 134001.

[32] LIGO Virgo Collaboration and ANTARES and IceCube Collaborations. (2016). High-energy Neutrino Follow-up Search of Gravitational Wave Event GW150914 with ANTARES and IceCube. *Phys. Rev. D* 93 122010.

[33] LIGO Virgo Collaboration. (2016). GW150914: The Advanced LIGO Detectors in the Era of First Discoveries. *Phys. Rev. Lett.* 116, 131103.

[34] LIGO Virgo, ASKAP, BOOTES, Dark Energy Survey and Camera, GW-EM, Fermi GBM and LAT, GRAWITA, INTEGRAL, IPTF, InterPlanetary, J-GEM, La Silla-Quest, Liverpool Telescope, LOFAR, MASTER, MAXI, MWA, PAN-STARRS, PESSTO, PI of the Sky, SkyMapper, Swift, TAROT, Zadko, Algerian National Observatory, C2PU, TOROS, and VISTA Collaborations. (2016). Localization and Broadband Follow-up of the Gravitational-wave Transient GW150914. *Astrophys. J. Lett.* 826, L13.

[35] Martynov, D.V., et al. (2016). Sensitivity of the Advanced LIGO detectors at the beginning of gravitational wave astronomy. *Phys. Rev. D* 93, 112004.

[36] Miller, Jeremy; Wardell, Barry; Pound, Adam. (2016). Second-order perturbation theory: the problem of infinite mode coupling. *arXiv:1608.0783v1.*

[37] Mino, Yasushi; Sasaki, Misao; Tanaka, Takahiro. (1996). Gravitational Radiation Reaction to a Particle Motion. *arXiv:gr-qc/9606018v1.*

[38] Misner, Charles W.; Thorne, Kip S.; Wheeler, John Archibald. (1973). *Gravitation.* W. H. Freeeman and Company.

[39] Newman, Mark. (2013). *Computational Physics.* University of Michigan.

[40] Philipp, Dennis; Perlick, Volker. (2015). On analytic solutions of wave equations in regular coordinate systems on Schwarzchild background. *arXiv:1503.08101v1*

[41] Poisson, Eric; Pound, Adam; Vega, Ian. (2011). The motion of point particles in curved spacetime. *Living Reviews in Relativity.* 14, 7.

[42] Pound, Adam. (2012). Second-order gravitational self-force. *arXiv:1201.5089v2.*

[43] Pound, Adam. (2017). Nonlinear gravitational self-force: second-order equation of motion. *arXiv:1703.02836v1.*

[44] Pound, Adam; Poisson, Eric. (2008). Osculating orbits in Schwarzschild spacetime, with an application to extreme mass-ratio inspirals. *Phys. Rev. D* 77, 044013.

[45] Press, William H.; Teukolsky, Saul A.; Vetterling, William T.; Flannery, Brian P. (2002). *Numerical Recipes in C++: The Art of Scientific Computing.* The Press Syndicate of the University of Cambridge.

[46] Price, Richard H. (1972). Nonspherical Perturbations of Relativistic Gravitational Collapse. I Scalar and Gravitational Perturbations. *Phys. Rev. D* 5, 10.

[47] Quinn, Theodore, C. (2000). Axiomatic approach to radiation reaction of scalar point particles in curved spacetime. *arXiv:qr-qc/0005030v1.*

[48] Quinn, Theodore C.; Wald, Robert M. An Axiomatic approach to electromagnetic and gravitational radiation reaction of particles in curved spacetime. *arXiv:gr-qc/9610053v1.*

[49] Saulson, Peter R. (1994). *Fundamentals of Interferometric Gravitational Wave Detectors.* World Scientific Publishing Co.

[50] Vega, Ian; Diener, Peter; Tichy, Wolfgang; Detweiler, Steven. (2009). Self-force with (3+1) codes: a primer for numerical relativists. *arXiv:0908.2138v1.*

[51] Vega, Ian; Wardell, Barry; Diener, Peter. (2011). Effective source approach to self-force calculations. *arXiv:1101.2925v1.*

[52] Vega, Ian; Wardell, Barry; Diener, Peter; Cupp, Samuel; Haas, Roland. (2013). Scalar self-force for eccentric orbits around a Schwarzschild black hole. *arXiv:1307.3476v2.*

[53] Vega, Ian; Wardell, Barry; Diener, Peter; Cupp, Samuel; Hass, Roland. (2013). Scalar self-force for eccentric orbits around a Schwarzschild black hole. *arXiv:1307.3476v2.*

[54] Volonteri, Marta. (2010). Formation of Supermassive Black Holes. *arXiv:1003.4404v1.*

[55] Wald, Robert M. (1984). *General Relativity.* The University of Chicago.

[56] Wardell, Barry. (2015). Self-Force: Computational Strategies. *arXiv:1501.07322v3.*

[57] Wardell, Barry; Vega, Ian; Thornburg, Jonathan; Diener, Peter. (2012). Generic effective source for scalar self-force calculations. *arXiv:1112.6355v3.*

[58] Wolfram, Stephen. (2016). *An Elementary Introduction to the Wolfram Language.* Wolfram-Media, inc.

[59] Yang, Huan; Zimmerman, Aaron; Zenginoglu, Anil; Zhang, Fan; Berti, Emanuele; Chen, Yanbei. (2013). Quasinormal modes of nearly extremal Kerr spacetimes: spectrum bifurcation and power-law ringdown. *arXiv:1307.8086v1.*

[60] Yunes, Nicolas; Wofgang, Tichy; Owen, Benjamin J.; Briigmann, Bernd. (2006). Binary black hole initial data from matched asymptotic expansions. *arXiv:gr-qc/0503011v3.*

[61] Yusef-Zadeh, F.; Wardle, M.; Schödel, R.; Roberts, D. A.; Cotton, W.; Bushouse, H.; Arendt, R.; Royster, M. (2016). SGR A^* and its environtment: Low-mass star formation, the origin of X-ray gas, and collimated outflow. *Astro. Ph. Journal*, 819, 60.

[62] Zenginoglu, Anil; Khanna, Gaurav. (2011). Null infinity waveforms from extreme-mass-ratio inspirals in Kerr spacetime. *arXiv:1108.1816v2.*

Vita

My past research has been on comet photometry, x-ray bursts, gravitational lensing and cosmology, exoplanets, neutrino oscillations, theoretical particle physics, gravitational waves, gravity gradient noise, and fractional calculus. Most of my background is in simulation, whether statistical or theoretical. I think of myself as a computational physicist and a multi-messenger astronomer.

I have 27 publications or preprints thanks in part to my membership in the LIGO Scientific Collaboration from 2009 to 2011. I made significant contributions to five of these, four related to LIGO and one related to exoplanets. I have also had the opportunity to submit, unsuccessfully, an additional first author paper on the simulation of fractional order circuit devices with Gary Bohannan at Saint Cloud State University.

Now I am a fourth year graduate student at Louisiana State University, exactly were I intended to be. I have worked on LIGO during the time of three detections. I have had the opportunity to gain experience with multiple techniques for speeding up code with supercomputers in my classes. I have done a little research involving databases and and more involving numerical algorithms. I have the opportunity to continue to contribute to the field of general relativity and to participate in a department where my broad background in the connections between various fields of astronomy is valued. I have helped supervise undergraduate research progress and made a lesson plan for and taught a graduate class, once. This document contains the research I have produced in the last three years since I arrived on June 3, 2014 at LSU and began working with Peter Diener. These have been the best three years of my life.

When interpreting the name on this document, please understand that I am female to male transgendered and that my legal name is Susan Elaine Dorsher but that I go by Steven James Dorsher.